

 Open access • Posted Content • DOI:10.1101/2021.07.24.453632

## **PTEN mutant NSCLC require ATM to suppress pro-apoptotic signalling and evade radiotherapy — [Source link](#)**

Thomas Fischer, Oliver Hartmann, Michaela Reissland, Cristian Prieto-Garcia ...+8 more authors

**Institutions:** University of Würzburg, Goethe University Frankfurt

**Published on:** 25 Jul 2021 - bioRxiv (Cold Spring Harbor Laboratory)

**Topics:** PTEN, PI3K/AKT/mTOR pathway, Ex vivo, Radiation sensitivity and DNA damage

Related papers:

- [PTEN inhibits non-small cell lung cancer cell growth by promoting G0/G1 arrest and cell apoptosis.](#)
- [Synergistic tumor suppression by adenovirus-mediated ING4/PTEN double gene therapy for gastric cancer](#)
- [Influence of human tumor suppressor PTEN on sensitivity of malignant cells to anticancer drugs](#)
- [Targeting human apurinic/apyrimidinic endonuclease 1 \(APE1\) in phosphatase and tensin homolog \(PTEN\) deficient melanoma cells for personalized therapy](#)
- [Effect of tumor suppressor gene PTEN on the resistance to cisplatin in human ovarian cancer cell lines and related mechanisms.](#)

Share this paper:    

View more about this paper here: <https://typeset.io/papers/pten-mutant-nsclc-require-atm-to-suppress-pro-apoptotic-ewc40xvdown>

1 PTEN mutant NSCLC require ATM to suppress pro-apoptotic signalling and evade  
2 radiotherapy

3

4 Thomas Fischer<sup>1,2,3</sup>, Oliver Hartmann<sup>2,3,\*</sup>, Michaela Reissland<sup>2,3\*</sup>, Cristian Prieto-  
5 Garcia<sup>2,3</sup>, Kevin Klann<sup>4</sup>, Christina Schülein-Völk<sup>5</sup>, Bülent Polat<sup>1,6</sup>, Elena Gerhard-  
6 Hartmann<sup>6,7</sup>, Mathias Rosenfeldt<sup>6,7</sup>, Christian Münch<sup>4</sup>, Michael Flentje<sup>1</sup> & Markus E.  
7 Diefenbacher<sup>2,3,‡</sup>

8

9

10 <sup>1</sup>Department of Radiation Oncology, University Hospital Würzburg, Würzburg, Germany

11 <sup>2</sup>Protein Stability and Cancer Group, University of Würzburg, Department of Biochemistry and Molecular Biology,  
12 Würzburg, Germany

13 <sup>3</sup>Mildred Scheel Early Career Center, Würzburg, Germany

14 <sup>4</sup>Protein Quality Control Group, Institute of Biochemistry II, Goethe University Frankfurt, Germany

15 <sup>5</sup>Core Unit High-Content Microscopy, Biocenter, University of Würzburg, Germany

16 <sup>6</sup>Comprehensive Cancer Centre Mainfranken, Würzburg, Germany

17 <sup>7</sup>Institute for Pathology, University of Würzburg, Germany

18

19 \*Equal contribution

20 ‡ Corresponding author

21

22 **Running Title:** PTEN loss establishes radiotherapy resistance

23

24 **Keywords:** PTEN, ATM, IR, NSCLC, Radiotherapy, Cancer. DNA-PK, PI3K.

25

26 \***Corresponding Author:** Dr. Markus E. Diefenbacher. Lehrstuhl für Biochemie und  
27 Molekularbiologie, Biozentrum, Am Hubland, Würzburg, 97074, Germany. Phone:  
28 0931 31-88167; Fax: 0931 31-84113; E-mail: [markus.diefenbacher@uni-](mailto:markus.diefenbacher@uni-wuerzburg.de)  
29 [wuerzburg.de](mailto:markus.diefenbacher@uni-wuerzburg.de)

30

31 **Conflict of Interest:** The authors declare no potential conflicts of interest.

32

33

34

35

36

37

38

39

40

41

42

43

44

45

46

47 **Abstract**

48

49 **Background**

50 Despite advances in treatment of patients with non-small cell lung cancer, carriers of  
51 certain genetic alterations are prone to failure. One such factor frequently mutated, is  
52 the tumor suppressor PTEN. These tumors are supposed to be more resistant to  
53 radiation, chemo- and immunotherapy.

54

55 **Methods**

56 Using CRISPR genome editing, we deleted PTEN in a human tracheal stem cell-like  
57 cell line as well generated primary murine NSCLC, proficient or deficient for *Pten*, *in*  
58 *vivo*. These models were used to verify the impact of PTEN loss *in vitro* and *in vivo*  
59 by immunohistochemical staining, western blot and RNA-Sequencing. Radiation  
60 sensitivity was assessed by colony formation and growth assays. To elucidate  
61 putative treatment options, identified via the molecular characterisation, PTEN pro-  
62 and deficient cells were treated with PI3K/mTOR/DNA-PK-inhibitor PI-103 or the  
63 ATM-inhibitors KU-60019 und AZD 1390. Changes in radiation sensitivity were  
64 assessed by colony-formation assay, FACS, western-blot, phospho-proteomic mass  
65 spectrometry and *ex vivo* lung slice cultures.

66

67 **Results**

68 We demonstrate that loss of PTEN led to altered expression of transcriptional  
69 programs which directly regulate therapy resistance, resulting in establishment of  
70 radiation resistance. While PTEN-deficient tumor cells were not dependent on  
71 DNA-PK for IR resistance nor activated ATR during IR, they showed a significant  
72 dependence for the DNA damage kinase ATM. Pharmacologic inhibition of ATM, via  
73 KU-60019 and AZD1390 at non-toxic doses, restored and even synergized with IR in  
74 PTEN-deficient human and murine NSCLC cells as well in a multicellular organotypic  
75 *ex vivo* tumor model.

76

77 **Conclusion**

78 PTEN tumors are addicted to ATM to detect and repair radiation induced DNA  
79 damage. This creates an exploitable bottleneck. At least *in cellulo* and *ex vivo* we  
80 show that low concentration of ATM inhibitor is able to synergise with IR to treat  
81 PTEN-deficient tumors in genetically well-defined IR resistant lung cancer models.

82

83

84

85

86

87

88

89

90

## 91 MATERIAL AND METHODS

92

### 93 Cell lines

94 Human BEAS-2B and HEK 293T cell lines was obtained from ATCC. Cells were  
95 maintained in high-glucose DMEM (Sigma Aldrich) supplemented with 10% FBS  
96 (Capricorn Scientific) and 1% Pen-Strep (Sigma Aldrich) 1% Glutamin (Sigma  
97 Aldrich) at 37°C in 5% CO<sub>2</sub> on 10 cm dishes (Greiner Bioscience). For cell  
98 detachment Trypsin (Sigma Aldrich) was used. All the cells were maintained in  
99 culture for 15 passages as maximum to maintain cell identity. Cells were routinely  
100 tested for mycoplasma via PCR. The reagents were dissolved in Dimethyl sulfoxide  
101 (DMSO) in specified concentrations and added to the cells.

102

### 103 DNA transfection and infection

104 For DNA transfection, a mix of 2,5 µg plasmid DNA, 200 µl free medium and 5 µl PEI  
105 was added into the 6-well dish medium (60% confluence), after 6 h incubation at  
106 37°C the medium was changed to full supplemented medium. For DNA infection  
107 retroviruses or lentiviruses (MOI=10) were added to the cell medium in the presence  
108 of polybrene (5µg/ml) and incubated at 37°C for 72 h. After incubation, infected cells  
109 were selected with 2 µg/ml puromycin for 72 h or 20 µg/ml blasticidin for 10 days.

110

### 111 X-ray irradiation

112 Irradiation was performed at room temperature using a 6 MV Siemens linear  
113 accelerator (Siemens, Concord, CA) at a dose rate of 9,5 Gy/min.

114

### 115 Colony forming

116 Dependent on the experiment cells were treated with two different protocols. With  
117 the direct seeding protocol exponential growing cells were seeded to 10 cm dishes in  
118 adequate amount to be 50-80% confluent next day. Cells were trypsinized, counted  
119 and diluted. The dilution was dispensed into different vials and cells were irradiated  
120 in suspension. Cells were directly seeded in adequate amounts into 10 cm plates to  
121 obtain 100-400 colonies per dish. With the re-seeding protocol exponential growing  
122 cells were seeded to 10 cm dishes in adequate amount to be 25-30% confluent next  
123 day. The attached cells were treated with different substances or DMSO as a control.  
124 3 h after treatment cells were irradiated with 0, 2, 3, 5, 7, 8 Gy and cultured for 24 h,  
125 then cells were trypsinized, counted and re-seeded in adequate amounts into 10 cm  
126 plates to obtain 100-400 colonies per dish. For both protocols KP and KPP cells  
127 formed colonies after 6 days, BEAS-2B cells formed colonies after 10-11 days. Cells  
128 were fixed with ice cold 25% acidic acid in methanol and stained with 0,5% crystal  
129 violet. Colonies were count manually. Only colonies containing at least 50 cells were  
130 scored. Surviving fractions were calculated by dividing the plating efficiency for the  
131 specified dose divided by the plating efficiency of untreated cells. Radiation  
132 treatment survival curves were fitted to the linear-quadratic model formula  $S = \exp[-\alpha D - \beta D^2]$  ( $S$ =survival fraction;  $D$ =radiation dose;  $\alpha$  and  $\beta$  fitted parameters). Curves  
133 were fitted and blotted using a non-linear regression and analysed with OriginPro  
134

135 (OriginPro, 2020, OriginLab Corporation, Northampton, MA, USA). Mean survival  
136 fractions at 2 Gy (SF2) and 4 Gy (SF4) were also obtained for each cell model and  
137 each substance and used to calculate the radiation enhancement ratio at 2 Gy  
138 ( $RER_{2Gy}$ ) and 4 Gy ( $RER_{4Gy}$ ) RER greater than 1 indicates enhancement of  
139 radiosensitivity, RER below the value of 1 indicates a radio resistance effect.  
140 Similarly, the radiation dose with 25% ( $D_{25}$ ) and 50% ( $D_{50}$ ) survival under different  
141 conditions was calculated to obtain the dose enhancement ratio ( $DER_{25}$  and  $DER_{50}$ )  
142 that is calculated by dividing  $D_{25}$  without substance treatment by  $D_{25}$  with substance  
143 treatment, respectively  $D_{50}$  without substance treatment by  $D_{50}$  with substance. DER  
144 greater than 1 indicates a radio sensitising effect, a DER below the value of 1  
145 indicates a radio protecting effect. Plating efficiency was calculated by dividing the  
146 number of colonies by the number of seeded cells. All calculated parameters are  
147 listed in supplementary table 1 (Table S1)

148

### 149 **Immunological methods**

150 Cells were lysed in RIPA lysis buffer (20 mM Tris-HCl pH 7.5, 150 mM NaCl, 1 mM  
151 Na<sub>2</sub>EDTA, 1 mM EGTA, 1% NP-40 and 1% sodium deoxycholate), containing  
152 proteinase inhibitor and phosphatase inhibitor (1/100; Bimake) by sonication using  
153 Branson Sonifier 150 with a duty cycle at 25%, output control set on level 2 and the  
154 timer set to 15 s. Protein concentration was quantified using Bradford assay (Biorad).  
155 After mixing of Bradford reagent with 2  $\mu$ l of sample, the photometer was used to  
156 normalize the protein amounts with a previously performed bovine serum albumin  
157 (BSA) standard curve. The quantified protein (40-80  $\mu$ g) was heated in 4x sample  
158 buffer (Thermo Fisher) and 10% sample reducing agent (Thermo Fisher) for 10 min  
159 at 70°C and separated on 4-12% Bis/Tris-gels or 3-8% Tris/Acetate-Gels (Thermo  
160 Fisher). After separation, protein was transferred to nitrocellulose membrane  
161 (Thermo Fisher) in transfer buffer (Thermo Fisher) and then, incubated with blocking  
162 buffer (5% low fat milk powder in TBS and 0.1% Tween20) for 60 min at RT. After  
163 blocking, membranes were incubated with indicated Primary antibodies (1/1000  
164 dilution in a buffer composed 5% low fat milk powder or 5% BSA in TBS and 0.1%  
165 Tween20) over night at 4°C. Secondary HRP coupled antibody (Dako 1/1000 dilution  
166 in a buffer composed 5% low fat milk powder or 5% BSA in TBS and 0.1% Tween20)  
167 were incubated for 2 h at 4°C. Membranes were incubated for 5 min in luminol-  
168 solution (250 mg luminol in 100 mM Tris pH 8,6) with 10% v/v cumarinic acid solution  
169 (1,1 g cumarinic acid in DMSO and 0,1% v/v H<sub>2</sub>O<sub>2</sub>) at RT, then membranes were  
170 recorded with my ECL Imaging System. Analysis and quantifications of protein  
171 expression was performed using Image Studio software (Licor Sciences, Lincoln,  
172 NE, USA). Antibodies used for this publication are listed in supplementary table 2  
173 (Table S2)

174

### 175 **AnnexinV/DAPI staining:**

176 Cells growing as sub-confluent monolayers were pretreated with substance for 3 h  
177 before radiation with 0 Gy and 8 Gy. The cells were kept under standard conditions  
178 for normal cell growth. 24 h, 48 h, 72 h and 96 h after radiation cells were harvested

179 with trypsinization. Non irradiated cells, treated with camptothecin 5  $\mu$ M (CPT) were  
180 harvested 48 h after treatment. Supernatant of cell culture dishes was pooled with  
181 trypsinized cells and pelleted by centrifugation. Further preparation for FACS  
182 measurement was following the protocol of the BioLegend APC Annexin V Apoptosis  
183 Detection Kit and DNA-staining with DAPI Reagent (25  $\mu$ g/mL) (Biolegend, San  
184 Diego, CA, USA). 20 000 cells were assayed using a flow cytometer FACSCantoll  
185 (Becton Dickinson, San Jose, CA, USA). The output data presented as two-  
186 dimensional dot plot. Samples were analyzed using the Flowing software gating  
187 events to avoid debris, then dividing events in four quadrants. Flowing software was  
188 obtained from P. Terho (Turku Centre for Biotechnology, Turku, Finland). Column  
189 histograms and statistics were analyzed with Graphpad PRISM 8 (GraphPad  
190 Software, San Diego, California USA) and OriginPro. (OriginPro, 2020, OriginLab  
191 Corporation, Northampton, MA, USA).

192

### 193 **sgRNA design**

194 sgRNAs were designed using the CRISPRtool ([https://zlab.bio/guide-design-](https://zlab.bio/guide-design-resources)  
195 [resources](https://zlab.bio/guide-design-resources)).

196

### 197 **AAV and lentivirus production and purification**

198 Virus was packaged and synthesized in HEK 293T cells seeded in 15 cm-dishes.

199 For AAV production, cells (70% confluence) were transfected with the plasmid of  
200 interest (10  $\mu$ g), pHelper (15  $\mu$ g) and pAAV-DJ or pAAV-2/8 (10  $\mu$ g) using PEI  
201 (70  $\mu$ g). After 96 h, the cells and medium of 3 dishes were transferred to a 50 ml  
202 Falcon tube together with 5 ml chloroform. Then, the mixture was shaken at 37°C for  
203 60 min and NaCl (1 M) was added to the mixture. After NaCl is dissolved, the tubes  
204 were centrifuged at 20 000 x g at 4°C for 15 min and the chloroform layer was  
205 transferred to another Falcon tube together with 10% PEG8000. As soon as the  
206 PEG800 is dissolved, the mixture was incubated at 4°C overnight and pelleted at 20  
207 000 x g at 4°C for 15 min. The pellet was resuspended in PBS with MgCl<sub>2</sub> and  
208 0.001% pluronic F68, then, the virus was purified using Chloroform and stored at -  
209 80C. AAV viruses were titrated using Coomassie staining and RT-PCR using AAV-  
210 ITR sequence specific primers.

211 For Lentivirus production, HEK 293T cells (70% confluence) were transfected with  
212 the plasmid of interest (15  $\mu$ g), pPAX (10  $\mu$ g) and pPMD2 (10  $\mu$ g) using PEI (70  $\mu$ g).  
213 After 96h, the medium containing lentivirus was filtered and stored at -80°C.

214

### 215 **In vivo experiments and histology**

216 All *in vivo* experiments were approved by the Regierung Unterfranken and the ethics  
217 committee under the license numbers 2532-2-362, 2532-2-367, 2532-2-374 and  
218 2532-2-1003. The mouse strains used for this publication are listed. All animals are  
219 housed in standard cages in pathogen-free facilities on a 12 h light/dark cycle  
220 with *ad libitum* access to food and water. FELASA2014 guidelines were followed for  
221 animal maintenance.

222

223 Adult mice were anesthetized with Isoflurane and intratracheally intubated with 50  $\mu$ l  
224 AAV virus ( $3 \times 10^7$  PFU) as previously described (Prieto-Garcia et al. 2019). Viruses  
225 were quantified using Coomassie staining protocol<sup>1</sup>. Animals were sacrificed by  
226 cervical dislocation and lungs were fixed using 10% NBF. H&E, slides were de-  
227 paraffinized and rehydrated following the protocol: 2x 5 min. Xylene, 2x 3 min. EtOH  
228 (100%), 2x 3 min. EtOH (95%), 2x 3 min. EtOH (70%), 3 min. EtOH (50%) and 3  
229 min. H<sub>2</sub>O. For all staining variants, slides were mounted with 200  $\mu$ l of Mowiol® 40-  
230 88 covered up by a glass coverslip. IHC slides were recorded using Panoramic  
231 DESK scanner or using FSX100 microscopy system (Olympus) and analysed using  
232 Case Viewer software (3DHISTECH) and ImageJ.

233

### 234 **Primary murine lung cancer cell lines**

235 In brief, at endpoint of experiment, tumor bearing mice were sacrificed and lung  
236 lobes excised. The tissue was briefly rinsed in PBS and transferred to PBS  
237 containing Petri dishes. By using a binocular, macroscopically detectable tumor  
238 lesions on the lung lobes were excised with a scissor and transferred to a test tube  
239 containing Collagenase I (100 U/ml in PBS). The tumor containing tissue was  
240 digested for 30 min at 37°C, and the reaction was stopped by addition of 10% FCS.  
241 The tissue/collagenase/FCS mixture was briefly spun in a benchtop centrifuge and  
242 the supernatant discarded. Digested tissue was re-suspended in 10% FCS  
243 (Capricorn) DMEM (Sigma Aldrich), Pen/Strep (Sigma Aldrich) and washed 3 times  
244 in 1 ml solution prior to plating in a 6 well tissue culture plate. During subsequent re-  
245 plating fibroblasts were counter-selected, by selective trypsinisation, and cell clusters  
246 with a homogenous morphology were clonally expanded. These clones were then  
247 subjected to further biochemical analysis and characterisation, including genotyping  
248 PCR, RNA-sequencing.

249

### 250 **Tumor area**

251 FFPE fixed tissue sections from animals were de-paraffinized and stained with  
252 haematoxylin and eosin (H&E). Each slide was scanned using a Roche Ventana  
253 DP200 slide scanner. To assess tumor area per animal, total lung area was  
254 measured by using the QuPath image analysis tool. Subsequently, all tumor nodules  
255 were measured and the tumor surface calculated. Graph was generated using  
256 GraphPad Prism 8.

257

### 258 **Survival curves mouse**

259 Upon intratracheal administration of AAV, animals were monitored on a daily basis.  
260 Whenever experimentally defined termination points were reached, such as 20%  
261 weight loss, animals were sacrificed by cervical dislocation and tissue samples  
262 collected. Graphs were generated using Prism Graphpad 8.

263

### 264 **RNA-sequencing**

265 RNA sequencing was performed with Illumina NextSeq 500 as described  
266 previously<sup>2</sup>. RNA was isolated using ReliaPrep™ RNA Cell Miniprep System

267 Promega kit, following the manufacturer's instruction manual. mRNA was purified  
268 with NEBNext® Poly(A) mRNA Magnetic Isolation Module (NEB) and the library was  
269 generated using the NEBNext® UltraTM RNA Library Prep Kit for Illumina, following  
270 the manufacturer's instructions).

271

### 272 **Sample preparation for mass spectrometry**

273 Lysates of cells, solved from cell culture plates with cell scrapers pelleted and frozen  
274 at -80°C, were precipitated by methanol/chloroform and proteins resuspended in 8 M  
275 Urea/10 mM EPPS pH 8.2. Concentration of proteins was determined by Bradford  
276 assay and 300 µg of protein per samples was used for digestion. For digestion, the  
277 samples were diluted to 1 M Urea with 10 mM EPPS pH 8.2 and incubated overnight  
278 with 1:50 LysC (Wako Chemicals) and 1:100 Sequencing grade trypsin (Promega).  
279 Digests were acidified using TFA and tryptic peptides were purified by Oasis Prime  
280 HLB columns (30 mg, Waters). 80 µg peptides per sample were TMTpro labeled,  
281 and the mixing was normalized after a single injection measurement by LC-MS/MS  
282 to equimolar ratios for each channel. 100 µg of pooled peptides were dried for offline  
283 High pH Reverse phase fractionation by HPLC (whole cell proteome) and remaining  
284 ~1.1 mg of multiplexed peptides were used for phospho-peptide enrichment by High-  
285 Select Fe-NTA Phosphopeptide enrichment kit (Thermo Fisher) after manufacturer`s  
286 instructions. After enrichment, peptides were dried and resuspended in 70%  
287 acetonitrile/0.1% TFA and filtered through a C8 stage tip to remove contaminating  
288 Fe-NTA particles. Dried phospho-peptides then were fractionated on C18 (Empore)  
289 stage-tip. For fractionation C18 stagetips were washed with 100% acetonitrile twice,  
290 followed by equilibration with 0.1% TFA solution. Peptides were loaded in 0.1% TFA  
291 solution and washed with water. Elution was performed stepwise with different  
292 acetonitrile concentrations in 0.1% Triethylamine solution (5%, 7.5%, 10%, 12.5%,  
293 15%, 17.5%, 20%, 22.5%, 25%, 27.5%, 30%, 50%). The resulting 12 fractions were  
294 concatenated into six fractions and dried for LC-MS.

295 Peptides were fractionated using a Dionex Ultimate 3000 analytical HPLC. 250 µg of  
296 pooled and purified TMT-labeled samples were resuspended in 10 mM ammonium-  
297 bicarbonate (ABC), 5% ACN, and separated on a 250 mm long C18 column (X-  
298 Bridge, 4.6 mm ID, 3.5 µm particle size; Waters) using a multistep gradient from  
299 100% Solvent A (5% ACN, 10 mM ABC in water) to 60% Solvent B (90% ACN, 10  
300 mM ABC in water) over 70 min. Eluting peptides were collected every 45 s into a  
301 total of 96 fractions, which were cross-concatenated into 24 fractions and dried for  
302 further processing.

### 303 **Liquid chromatography mass spectrometry**

304 All mass spectrometry data was acquired in centroid mode on an Orbitrap Fusion  
305 Lumos mass spectrometer hyphenated to an easy-nLC 1200 nano HPLC system  
306 using a nanoFlex ion source (ThermoFisher Scientific) applying a spray voltage of  
307 2.6 kV with the transfer tube heated to 300°C and a funnel RF of 30%. Internal mass  
308 calibration was enabled (lock mass 445.12003 m/z). Peptides were separated on a  
309 self-made, 32 cm long, 75 µm ID fused-silica column, packed in house with 1.9 µm  
310 C18 particles (ReproSil-Pur, Dr. Maisch) and heated to 50°C using an integrated



311 column oven (Sonation). HPLC solvents consisted of 0.1% Formic acid in water  
312 (Buffer A) and 0.1% Formic acid, 80% acetonitrile in water (Buffer B).

313 For total proteome analysis, a synchronous precursor selection (SPS) multi-notch  
314 MS3 method was used in order to minimize ratio compression as previously  
315 described. Individual peptide fractions were eluted by a non-linear gradient from 7 to  
316 40% B over 90 min followed by a step-wise increase to 95% B in 6 min which was  
317 held for another 9 min. Full scan MS spectra (350-1400 m/z) were acquired with a  
318 resolution of 120,000 at m/z 200, maximum injection time of 100 ms and AGC target  
319 value of  $4 \times 10^5$ . The most intense precursors with a charge state between 2 and 6  
320 per full scan were selected for fragmentation and isolated with a quadrupole isolation  
321 window of 0.7 Th and a cycle time of 1.5 s. MS2 scans were performed in the Ion  
322 trap (Turbo) using a maximum injection time of 50 ms, AGC target value of  $1.5 \times 10^4$   
323 and fragmented using CID with a normalized collision energy (NCE) of 35%. SPS-  
324 MS3 scans for quantification were performed on the 10 most intense MS2 fragment  
325 ions with an isolation window of 0.7 Th (MS) and 2 m/z (MS2). Ions were fragmented  
326 using HCD with an NCE of 65% and analyzed in the Orbitrap with a resolution of  
327 50,000 at m/z 200, scan range of 110-500 m/z, AGC target value of  $1.5 \times 10^5$  and a  
328 maximum injection time of 120 ms. Repeated sequencing of already acquired  
329 precursors was limited by setting a dynamic exclusion of 45 seconds and 7 ppm and  
330 advanced peak determination was deactivated.

331 For phosphopeptide analysis, each peptide fraction was eluted by a linear gradient  
332 from 5 to 32% B over 120 min followed by a step-wise increase to 95% B in 8 min  
333 which was held for another 7 min. Full scan MS spectra (350-1400 m/z) were  
334 acquired with a resolution of 120,000 at m/z 200, maximum injection time of 100 ms  
335 and AGC target value of  $4 \times 10^5$ . The most intense precursors per full scan with a  
336 charge state between 2 and 5 were selected for fragmentation, isolated with a  
337 quadrupole isolation window of 0.7 Th and fragmented via HCD applying an NCE of  
338 38% with an overall cycle time of 1.5 s. MS2 scans were performed in the Orbitrap  
339 using a resolution of 50,000 at m/z 200, maximum injection time of 86ms and AGC  
340 target value of  $1 \times 10^5$ . Repeated sequencing of already acquired precursors was  
341 limited by setting a dynamic exclusion of 60 s and 7 ppm and advanced peak  
342 determination was deactivated.

343

## 344 **QUANTIFICATION AND STATISTICAL ANALYSIS**

### 345 *RNA-sequencing analysis*

346 Fastq files were generated using Illuminas base calling software GenerateFASTQ  
347 v1.1.0.64 and overall sequencing quality was analyzed using the FastQC script.  
348 Reads were aligned to the human genome (hg19) using Tophat v2.1.1<sup>3</sup> and Bowtie2  
349 v2.3.2<sup>4</sup> and samples were normalised to the number of mapped reads in the smallest  
350 sample. For differential gene expression analysis, reads per gene (Ensembl gene  
351 database) were counted with the “summarizeOverlaps” function from the R package  
352 “GenomicAlignments” using the “union”-mode and non- or weakly expressed genes  
353 were removed (mean read count over all samples <1). Differentially expressed  
354 genes were called using edgeR<sup>5</sup> and resulting p-values were corrected for multiple

355 testing by false discovery rate (FDR) calculations. GSEA analyses were done with  
356 signal2Noise metric and 1000 permutations. Reactome analysis were performed with  
357 PANTHER<sup>6</sup> using the “Statistical overrepresentation test” tool with default settings.  
358 Genes were considered significantly downregulated for Reactome analysis when:  
359 Log2FC>0.75 and FDR p-value<0.05.

#### 360 *Analysis of publicly available data*

361 All publicly available data and software used for this publication are listed (please  
362 see Star Methods). Oncoprints were generated using cBioportal<sup>7, 8</sup>. Briefly,  
363 Oncoprints generates graphical representations of genomic alterations, somatic  
364 mutations, copy number alterations and mRNA expression changes. TCGA data was  
365 used for the different analysis. Data were obtained using UCSC Xena. Data was  
366 downloaded as log2 (norm\_count+1)

367  
368 Kaplan-Meier curves were estimated with the KM-plotter<sup>9</sup>, cBioportal<sup>7</sup> and R2:  
369 Genomics Analysis and Visualization Platform (<http://r2.amc.nl>). The KM-plotter was  
370 used to analyse overall survival of lung cancer patients (Figure 1 and S1) based on  
371 gene expression data from microarrays obtained from GEO, caBIG and TCGA

#### 372 373 *Mass spectrometry data analysis*

374 Raw files were analyzed using Proteome Discoverer (PD) 2.4 software  
375 (ThermoFisher Scientific). Spectra were selected using default settings and  
376 database searches performed using SequestHT node in PD. Database searches  
377 were performed against trypsin digested Mus musculus SwissProt database  
378 containing one sequence per gene without isoforms. Static modifications were set as  
379 TMTpro at the N-terminus and lysines and carbamidomethyl at cysteine residues.  
380 Search was performed using Sequest HT taking the following dynamic modifications  
381 into account: Oxidation (M), Phospho (S,T,Y), Met-loss (Protein N-terminus), Acetyl  
382 (Protein N-terminus) and Met-loss acetyl (Protein N-terminus). For whole cell  
383 proteomics, the same settings were used except phosphorylation was not allowed as  
384 dynamic modification. For phospho-proteomics all peptide groups were normalized  
385 by summed intensity normalization and then analyzed on peptide level<sup>10</sup>. For whole  
386 cell proteomics normalized PSMs were summed for each accession and data  
387 exported for further use. For proteomics analysis, significance was assessed via a  
388 two-sided unpaired students t-test with equal variance assumed. For pathway  
389 analysis, Protein/Peptide lists were filtered as indicated and a STRING network  
390 created in Cytoscape. For the resulting network a pathway enrichment analysis was  
391 performed using the STRING App Cytoscape plugin. For network views of  
392 enrichments, the Reactome pathways were filtered for a FDR < 0.001 and loaded  
393 into the Enrichment Map 3 plugin for Cytoscape to create visualization. Gene sets for  
394 visualization purposes were downloaded from the molecular signature gene set  
395 database (<https://www.gsea-msigdb.org/>) on 02-21-2021. Result files were filtered  
396 for the included genes to create pathway specific visualizations.

397

#### 398 **DATA AND SOFTWARE AVAILABILITY**

399 Raw data is available via Mendeley Data: doi: RNA-sequencing data is available at  
400 the Gene Expression Omnibus under the accession number GEO:

401

402 **Contact for reagent and resource sharing**

403 Further information and requests for resources and reagents should be directed to  
404 and will be fulfilled by the Lead Contact, Markus E. Diefenbacher  
405 ([markus.diefenbacher@uni-wuerzburg.de](mailto:markus.diefenbacher@uni-wuerzburg.de)).

406

407

408

409

410

411

412

413

414

415

416

417

418

419

420

421

422

423

424

425

426

427

428

429

430

431

432

433

434

435

436

437

438

439

440

441

442

443

444

## 445 **Introduction**

446 Lung cancer is the most common cancer worldwide, claiming 1.76 million lives in  
447 2018 alone (WHO cancer statistics 2018). This is exceeding total numbers of colon,  
448 breast and prostate cancer combined<sup>11-14</sup>. In the past decade, with the advent of  
449 targeted and immune-checkpoint blockade therapy, major improvements in  
450 treatment response of advanced NSCLC (non-small cell lung cancer) were  
451 achieved<sup>15</sup>. Targeted therapies are predominantly validated in the treatment of late  
452 stage patients (UICC stage IV)<sup>16</sup>. Other patients (UICC stage I, II and III)<sup>17</sup>, rarely  
453 benefit from these combinatorial treatments and survival rates have only marginally  
454 improved, with many patients still succumb to lung cancer within five years<sup>18</sup>.  
455 Furthermore, not all patients benefit equally from these novel therapeutic  
456 approaches<sup>19-21</sup>. Genetic analysis of tumor samples by Next Generation Sequencing  
457 (NGS) from treatment resistant patients highlighted that several genetic alterations  
458 can contribute to therapy resistance and reduced patient survival e.g. *KRAS*, *STK11*,  
459 *KEAP1* and the phosphatase and tensin homologue (*PTEN*)<sup>22-24</sup>.

460

461 *PTEN* was initially described as a phosphatase involved in the homeostatic  
462 maintenance of the phosphatidylinositol-3-kinase/protein kinase B (PI3K/AKT)  
463 cascade leading to suppression of phospho-AKT<sup>25</sup>. It functions as a tumor  
464 suppressor via affecting cell cycle progression, inhibition of cell death, transcription,  
465 translation, stimulation of angiogenesis, and maintenance of stem cell self-properties  
466 via mTOR signalling<sup>26</sup>. NGS of tumor samples revealed that *PTEN* is frequently  
467 deleted or mutated in a variety of tumors<sup>12</sup>, including NSCLC (Adenocarcinoma and  
468 Squamous cell carcinoma)<sup>13, 14</sup>. *PTEN* itself, as a tumor suppressor, is not a direct  
469 target for cancer therapy, but can serve as a prognostic marker<sup>27</sup>. Mutations in *PTEN*  
470 result in resistance towards 'standard of care' therapies, such as radiotherapy and  
471 chemotherapy, by hyperactivation of the AKT pathway<sup>28</sup>. Additionally, loss of *PTEN*  
472 limits the employment of personalized therapy, as it is blunting therapeutic  
473 responses relying on immune checkpoint blockade and drives resistance to  
474 established targeted therapies like EGFR antagonists<sup>29, 30</sup>. Nuclear *PTEN* is involved  
475 in the control of essential biological processes, such as maintenance of genome  
476 integrity<sup>31</sup>, APC/C-CDH1-dependent PLK and AURK degradation<sup>32</sup>, chromatin  
477 remodelling<sup>33</sup> and double strand break repair<sup>34</sup>.

478

479 DNA damage inducing therapies, such as ionizing radiation (IR), rely on the inability  
480 of tumor cells to efficiently clear all damage, while wild type cells undergo cell cycle  
481 arrest to gain sufficient time to repair<sup>35, 36</sup>. Here, DNA damage sensing enzymes,  
482 such as DNA-PK, ATR and ATM are key players and dictate the route taken for  
483 repair of the damaged DNA<sup>37, 38</sup>. Ataxia telangiectasia mutated kinase (ATM) is the  
484 prime sensor of double strand breaks induced by ionizing radiation<sup>38</sup>. It is required  
485 for downstream activation of SMC1, CHEK2, RAD50-MRE11 and BRCA1 signalling

486 cascades, thereby contributing to radiation resistance and cell cycle checkpoint  
487 progression and arrest<sup>39</sup>. An alternative source of ATM activation is the induction of  
488 reactive oxygen species, a by-product of IR therapy<sup>40</sup>. Previous reports also  
489 highlighted a deregulation of ATM in PTEN mutant tumors, suggesting that the ATM-  
490 PTEN axis is of therapeutic value for certain cancers<sup>41, 42</sup>. Together, these data  
491 argue that inhibition of DNA damage sensors may restore therapy responses in  
492 PTEN mutant NSCLC and suggest that this strategy may have therapeutic efficacy in  
493 lung cancer.

494

## 495 **Results**

496

### 497 ***Alterations in PTEN affect patient survival and radiation therapy outcome in*** 498 ***NSCLC***

499

500 To assess the mutational as well the expression status of PTEN in human  
501 malignancy, we analysed public available patient data. Alterations in PTEN were  
502 frequently observed in lung cancer, both in adenocarcinoma (ADC) and squamous  
503 cell carcinoma (SCC), ranging between 15% and 38%, respectively (Figure 1A).  
504 PTEN is frequently altered in invasive tumors and reduced expression or mutation  
505 correlate with overall shortened patient survival (Figure 1B and S1A). Irrespective of  
506 NSCLC subtype, patient data suggest that PTEN loss is a direct prognostic marker  
507 for shorter survival, including tumor mutational burden (TMB) low patients, which are  
508 otherwise not amenable to immunotherapy and treated with chemotherapy (Figure  
509 S1A). Not only do *PTEN<sup>mutant/low</sup>* patients have an overall shortened life expectancy;  
510 when treated with radiotherapy alone, they have a poorer overall survival  
511 ( $p=0,00017$ ) compared to a *PTEN<sup>high</sup>* patient cohort (Figure 1B). These data  
512 demonstrate that reduced expression or mutation of *PTEN* is a frequent event and  
513 significantly correlates with poor patient survival and treatment failure.

514

### 515 ***Radiation sensitivity is PTEN-dosage dependent***

516

517 Next, we investigated if loss of *PTEN* contributes to radiotherapy resistance. Instead  
518 of using classic human lung cancer cell lines with a high mutational burden, we  
519 utilized the human lung tracheal stem cell like cell line BEAS-2B. By using  
520 differentiated BEAS-2B cells we were on the one hand able to avoid putative  
521 mutations contributing to IR resistance, on the other hand we could mimic tumors  
522 with low TMB and worse patient survival outcome, with bigger need for successful  
523 treatment options. Deletion of PTEN in BEAS-2B was achieved by simultaneous  
524 CRISPR/Cas9 mediated gene editing of *PTEN* exon 1 and exon 4 (Figure 1C).  
525 BEAS-2B cells were lentivirally infected and upon Blasticidin selection, individual  
526 clones were analysed (Figure S1B). CRISPR/Cas9 mediated genome editing yielded  
527 heterozygous as well as homozygous deletions of *PTEN*, as seen by immunoblotting  
528 against endogenous PTEN (Figure 1D). As previously reported, loss of PTEN led to  
529 enhanced phosphorylation of AKT and its downstream target, S6 kinase, as seen by

530 western blotting (Figure 1D and E). It is noteworthy that heterozygous loss of PTEN  
531 was sufficient to activate downstream phosphorylation cascades. Generated clones  
532 were expanded and subjected to a single dose of ionizing radiation of 2, 3, 5, 7 or  
533 8 Gy, respectively. Upon irradiation, cells were directly re-seeded from suspension  
534 and colony formation capacity was assessed by crystal violet staining (Figure 1F,  
535 S1C and D). While  $PTEN^{wt}$  BEAS-2B demonstrated an IR dosage dependent ability  
536 to form colonies, clones depleted for PTEN,  $PTEN^{clone-II(het)}$  and  $PTEN^{clone-III(homo)}$ ,  
537 tolerated higher doses of IR, indicating that PTEN loss contributes to IR resistance  
538 (Figure 1F and S1D). Since mutations in PTEN co-occur with mutations in oncogenic  
539 drivers, we tested the impact of aberrant MAPK signalling on IR resistance (Figure  
540 1E and S1F). By retroviral transduction, a mutant form of BRAF,  $BRAF^{V600E}$ , was  
541 introduced in the clonal lines  $PTEN^{wt}$  and  $PTEN^{clone-III3(homo)}$  BEAS-2B.  
542 Overexpression of the mutant  $V600E$  variant of  $BRAF$  was detectable and resulted in  
543 the downstream activation of the MAPK pathway, as seen by phosphorylation of  
544 MEK (Figure S1E). Oncogenic  $BRAF^{V600E}$  did not alter the radiation sensitivity of  
545  $PTEN^{wt}$  BEAS-2B nor affected the relative resistance of  $PTEN^{homo}$  BEAS-2B (Figure  
546 S1F).

547

548 These data demonstrate that genetic loss or mutation of PTEN is sufficient to  
549 establish IR resistance in the human non-oncogenic cell line BEAS-2B.

550

### 551 ***Loss of Pten cooperates with mutant Tp53 and KRas<sup>G12D</sup> in murine NSCLC in*** 552 ***vivo and diminishes radiationsensitivity ex vivo***

553

554 To investigate if the observed IR resistance is limited to “stable” cell lines or is a  
555 ‘hardwired’ feature of PTEN mutant tumors, we used CRISPR-mediated NSCLC  
556 mouse models driven by either mutations of Tp53 and KRas (KP:  $KRas^{G12D}, Tp53^{mut}$ )  
557 and studied the impact of an additional deletion of Pten (KPP :  $KRas^{G12D}$   
558 :  $Tp53^{mut} : Pten^{mut}$ ). Constitutive Cas9 expressing mice were infected via intratracheal  
559 administration with an adeno-associated virus (AAV), packaged with the ubiquitous  
560 rep/cap 2/DJ<sup>43</sup>. 12 weeks post infection tumor burden and viability were assessed  
561 (Figure S2A). While  $KP$  mice developed tumors resulting in an overall transformation  
562 of around 16% of lung tissue, additional loss of  $Pten$  (KPP) proven by  
563 immunohistochemistry greatly enhanced the tumor area to 80% (Figure 2A, B and  
564 C). Additionally, as reported for patients, loss of  $Pten$  negatively affected survival  
565 (Figure 2D). While  $KP$  mice survived 12 weeks without showing physiological effects  
566 caused by their tumor burden,  $KPP$  mice required premature termination due to  
567 onset of various symptoms, such as weight loss/cachexia and increased breathing  
568 frequency (Figure 2D). Next, we established tumor cell lines from various animals by  
569 ectopic dissection of tumors and subsequent culture in standard medium  
570 (DMEM/10%serum/5%Pen/Strep)<sup>44</sup>. The genetic status of four established cell lines  
571 (KP5 and KP6;  $KRas^{G12D} : Tp53^{mut}$ ; KPP4 and KPP8;  $KRas^{G12D} : Tp53^{mut} : Pten^{mut}$ ) was  
572 confirmed by polymerase chain reaction of genomic DNA derived from tumor cells.  
573 Loss of  $Pten$  and activation of the downstream pathway was further confirmed by

574 immunoblotting and immunohistochemistry, showing increased phosphorylation of  
575 AKT in *KPP* when compared to *KP* tumors and primary tumor cell lines (Figure 2B, E  
576 and S2B and C). Exposure to IR significantly reduced the capacity of *KP* cells to  
577 establish colonies (Figure 2F). *KPP* tolerated higher doses of ionizing radiation  
578 compared to *Pten* wild type cells, reproducing the results obtained in the human cell  
579 line BEAS-2B *PTEN*<sup>homo</sup> (Figure 1F and 2F). Immunoblot analysis of pathway  
580 components of the PI3K and MAPK pathway of *KP* and *KPP* clones demonstrated  
581 that cells depleted of *Pten* maintained elevated expression of EGFR and  
582 phosphorylated AKT during ionizing irradiation, while other components of the  
583 pathway were not affected (Figure S2B and C).

584

585 For proof of principle, we reconstituted the radiation resistant clone *KPP4* with a  
586 human full length wild type *PTEN* cDNA, using lentiviral transduction (Figure 2G and  
587 S2D). *PTEN* expression was confirmed by immunoblotting against *Pten/PTEN*.  
588 Radiation dose response of several reconstituted clones was measured using colony  
589 survival. All clones expressing human *PTEN* showed enhanced sensitivity towards  
590 IR when compared to the parental *PTEN*<sup>mut</sup> clone (Figure 2H).

591

592 Our data demonstrate that loss of *Pten* synergises with loss of *Trp53* and oncogenic  
593 *KRas* in NSCLC and accelerated tumor growth in the mouse lung. Cell lines derived  
594 from these tumors and lacking *Pten* showed decreased radiation sensitivity.

595

### 596 ***Loss of Pten alters DNA damage signalling pathways***

597

598 To understand how *Pten* loss affects overall gene expression, and if these changes  
599 could account for the IR resistance of *PTEN*<sup>mutant</sup> cells, we performed transcriptomic  
600 analysis by RNA sequencing of *KP6* and *KPP4* (from here on *KP* and *KPP*). While  
601 *KP* and *KPP* derived tumor cells share a high degree of commonly regulated genes  
602 (Spearman R=0.9122, Figure 3A), *KPP* cells upregulated 2441 distinct genes when  
603 compared to *KP* (Figure 3B). Gene set enrichment analysis (GSEA) showed that *KP*  
604 cells are predominantly driven by the *KRas* pathway, while cells mutant for *PTEN*  
605 altered the transcriptional profile towards the *AKT1-mTOR* pathway (Figure S3A).  
606 Furthermore, *PTEN*<sup>mutant</sup> cells upregulated the expression of genes that correlate  
607 with radiation resistance, such as *SftpC*, *Slc34a2*, *Tub*, *Myh6* and *Shh*, while IR  
608 sensitizing genes, such as *Wisp2* and *Bex*, were enriched in *KP* tumors (Figure 3C).  
609 Additionally, *PTEN*<sup>mutant</sup> cells upregulate pathways associated with IR and  
610 Doxorubicin resistance (Figure 3D), both treatments resulting in double strand  
611 breaks. Genes associated with Telomere end packaging and maintenance were  
612 enriched in *PTEN*<sup>mutant</sup> cells compared to *KP* cells (Figure S3B). Overall, loss of *Pten*  
613 led to a transcriptomic shift towards pathways that are associated with  
614 aggressiveness, metastasis and therapy resistance (Figure 3D and S3A). This was  
615 further evidenced by increased expression of c-MYC (V1), E2F and reactive oxygen  
616 species (ROS) pathway genes in *KPP* tumor cells (Figure S3B).

617

618 *KPP* tumors appear to upregulate the DNA damage response already at steady  
619 state. To investigate if DNA damage recognition and clearance therefore varies  
620 between *Pten* proficient and deficient cells, we subjected *KP* and *KPP* cells to IR (8  
621 Gy) and studied radiation induced presence and activity state of DNA damage  
622 kinase ATR as seen by phosphorylation, (Figure S3E). While non-irradiated cells had  
623 low amounts of phospho-ATR, already 5 minutes' post IR exposure led to a  
624 significant and rapid increase of phospho-ATR in *KP* cells, while *KPP* failed to  
625 activate ATR (Figure S3C).

626 It is noteworthy that ATR is apparently not activated in *KPP* cells, while both cell  
627 lines upregulated  $\gamma$ H2AX. This is an intriguing observation that could point towards  
628 an efficient mechanism for DNA damage recognition and clearance, present in *Pten*  
629 deficient tumor cells. This could putatively contribute to the DNA damage therapy  
630 evasion frequently observed in *PTEN* mutant patients. Furthermore, the lack of ATR  
631 activation during IR exposure argues that loss of *PTEN* could rewire the DNA  
632 damage signalling network towards DNA-PK or ATM.

633

### 634 ***Interference with PI3K-mTORC signalling via the dual specific small molecule*** 635 ***inhibitor PI-103 in *PTEN*<sup>mutant</sup> cells***

636

637 Loss of *PTEN* interferes with the PI3K–mTOR signalling cascade, leading to  
638 constant phosphorylation of AKT. Phospho-AKT activates DNA-PK, a key enzyme in  
639 DNA-damage recognition and repair<sup>45, 46</sup>. Cells may develop addiction to this  
640 situation. To investigate whether this could serve as an exploitable vulnerability, we  
641 irradiated the primary murine NSCLC cell lines *KP* and *KPP* in the presence or  
642 absence of PI-103, a potent PI3K/AKT and mTOR inhibitor, that also interferes with  
643 DNA-PK (Figure 4A and S4A, B and <sup>47</sup>). Cells were pre-treated with 2  $\mu$ M PI-103 for  
644 3 h, followed by irradiation with 8 Gy. Whole protein extracts were collected at  
645 indicated time points post IR, followed by immunoblotting against total and  
646 phosphorylated AKT (Figure 4A and S4A). While whole protein levels as well as  
647 phosphorylated amounts of AKT were not altered in *KP* cells upon exposure to 8 Gy  
648 in presence or absence of PI-103, *KPP* cells showed pathway inhibition at time of  
649 irradiation and for at least two hours post irradiation, as seen by diminished  
650 phosphorylation of AKT (Figure 4A). However, the pathway was swiftly reactivated  
651 within 4 h post irradiation and AKT phosphorylation was fully restored (Figure 4A).  
652 This demonstrates that blockage of the PI3K-AKT pathway via PI-103 only effected a  
653 brief pathway inhibition in *Pten*<sup>mutant</sup> cells. Radiation dose dependent colony formation  
654 of *KPP* was not different in the presence of 2  $\mu$ M PI-103, while *KP* showed mild  
655 sensitization. (Figure 4B and S4B). To investigate the differential responses of *KP*  
656 and *KPP* cells to ionizing irradiation in the presence or absence of PI-103 treatment,  
657 next, we measured cell survival by trypan blue staining with an automated cell  
658 counter. Here, in a dose dependent fashion, overall cell numbers were reduced  
659 when cells were exposed to PI-103 (Figure 4C). The small molecule inhibitor did not  
660 induce cell death at lower concentrations but synergized with ionizing radiation in the  
661 *Pten* wild type cancer cell line *KP* in higher concentrations (10  $\mu$ M to 20  $\mu$ M), as



662 seen by a decrease in viable cells. The *Pten*<sup>mutant</sup> KPP cell line only demonstrated an  
663 initial growth disadvantage and a mild reduction in cell viability, however, tolerated  
664 higher concentrations of PI-103 in combination with IR than KP (Figure 4C).

665

666 Treatment of BEAS-2B cells revealed slightly differing results. While solvent/DMSO  
667 treated cells showed robust activation of the AKT-mTORC pathway, as  
668 demonstrated by phosphorylation of AKT and S6 in *PTEN*<sup>mutant</sup> cells, exposure to 2  
669  $\mu$ M PI-103 for 3 h inhibited AKT and significantly reduced phosphorylation of S6  
670 (Figure 4D). Dose dependent clonogenic survival upon IR in the presence of solvent  
671 control or PI-103 (Figure S4B) demonstrated, that treatment with PI-103 reduced IR  
672 resistance only to modest extent in PTEN deficient cells (both *PTEN*<sup>mutant</sup> and  
673 *PTEN*<sup>mutant</sup> BRAF<sup>V600E</sup>), while PTEN WT cells showed a distinct sensitisation to  
674 radiation (Figure 4E, S4C and D).

675

676 Our data demonstrate that combined PI3K, mTOR and DNA-PK inhibition is not an  
677 effective treatment to overcome *PTEN*<sup>mutant</sup> induced radiation resistance.

678

679 ***Inhibition of ATM kinase by KU-60019 or AZD 1390 restores IR sensitivity in***  
680 ***Pten*<sup>mut</sup> ***BEAS-2B and murine NSCLC cells*****

681

682 Next, we tested whether the DNA damage kinase ATM could present a target in  
683 *PTEN*<sup>mut</sup> cells. Two ATM inhibitors (KU-60019 and AZD 1390) were employed in our  
684 genetically engineered BEAS-2B and KP6 versus KPP4 cells (Figure 5A, B and S5A,  
685 B). Cells were treated with ATM inhibitor or solvent control for 27 hours (to model 3  
686 hours pre-treatment and 24 hours of IR and recovery time), then dose dependent  
687 colony survival was measured. KU-60019 and AZD 1390 had little effect on overall  
688 cell survival up to a concentration of 3  $\mu$ M in the tested cell lines, and growth  
689 inhibition was only observed in concentrations exceeding 10  $\mu$ M (Figure 5A, B and  
690 S5A, B). Immunoblotting of genetically engineered BEAS-2B as well as KP versus  
691 KPP cells showed that non-irradiated cells had very low levels of detectable  
692 phosphorylated ATM or  $\gamma$ H2AX (Figure 5C, D and S5C). Upon exposure to 8 Gy,  
693 phosphorylated ATM as well as  $\gamma$ H2AX were strongly increased in all analysed cell  
694 lines. Treatment with 0.3  $\mu$ M KU-60019 significantly reduced, and exposure to 3  $\mu$ M  
695 KU-60019 blocked the phosphorylation of ATM and led to a marked reduction in  
696 overall  $\gamma$ H2AX protein levels (Figure 5C, D). Loss of  $\gamma$ H2AX indicates that  
697 interference with ATM activation in irradiated cells impairs downstream DNA damage  
698 signalling. Comparable results were obtained when AZD 1390 was used (Figure  
699 S5C). In concentrations exciding 3 $\mu$ M, AZD 1390 interfered with AKT  
700 phosphorylation in *Pten* mutant cells, potentially via blocking PI3K (Figure S5C).

701

702 Next, we tested the combinatorial treatment of *PTEN/Pten* wild type and mutant cells  
703 with ATM inhibition and IR. To this end, cells were pre-treated with the indicated  
704 ATM inhibitors for 3 hours at nontoxic concentrations of 0.3  $\mu$ M or 3  $\mu$ M,  
705 respectively, followed by exposure to indicated doses of ionizing radiation. Cells

706 were re-seeded and colony formation capacity was analysed. Exposure of  
707 *PTEN/Pten* mutant cells to ATM inhibitor, in an ATM-inhibitor dosage dependent  
708 fashion, resulted in radio-sensitization and reduction of clonogenic survival (Figure  
709 5E, F and S5D, E). Comparable results were obtained when AZD 1390 was used  
710 (Figure S5F). It is note worth noting that the expression of oncogenic *BRAF*<sup>V600E</sup> did  
711 not alter the response of *PTEN* mutant cells to combinatorial treatment (Figure S5E).

712

713 These data demonstrate that ionizing radiation resistant *PTEN*<sup>mutant</sup> cells are  
714 addicted to the DNA damage kinase ATM. This tumor bottleneck can be exploited,  
715 as wild type nor tumor cells relied on active ATM for cell proliferation, at least *ex*  
716 *vivo*, and tolerated ATM inhibition via KU-60019 or AZD 1390, while in combination  
717 with ionizing radiation, *PTEN*<sup>mutant</sup> cells, human and murine, succumbed to therapy

718

### 719 ***Pten*<sup>mut</sup> NSCLC require ATM to suppress a pro-apoptotic program upon IR**

720

721 To gather further insights into how loss of *Pten/PTEN* reshapes the cellular  
722 responses upon ionizing radiation, we compared global changes in the appearance  
723 of phosphorylation, a major post-translational modification, required to regulate the  
724 activity of several key enzymes of the DNA damage response (DDR) and apoptosis  
725 signalling cascade<sup>37, 48, 49</sup>.

726 Analysis of the global phospho-proteome revealed fundamental differences between  
727 *Pten* proficient and deficient cell lines (Figure 6A and S6A). Already under basal  
728 conditions pathways associated with RNA splicing, apoptosis, RNA polymerase and  
729 stress responses were differentially regulated (Figure 6A and S6A). These steady-  
730 state differences might influence the reaction of these cells to stressors, such as  
731 radiation. Exposure to IR differentially regulated pathways associated with cell cycle  
732 and G2/M checkpoints, but also RNA Pol I & II, mRNA processing and TP53 activity  
733 or apoptosis (Figure 6B). Comparative phospho-proteomic analysis revealed a small  
734 cluster of apoptotic hallmark genes (MSigDB), differentially regulated after IR in *Pten*  
735 deficient cells (Figure 6C). Addition of ATM inhibitor KU-60019 resolved this  
736 deregulated cluster towards a *Pten* proficient like response (Figure 6C). Analysis of  
737 this cluster showed that pro-apoptotic proteins, such as Rara, Caspase 8, Diablo,  
738 Bax and Bcl2l1 were less phosphorylated in *Pten* deficient cells upon exposure to IR,  
739 hence, pro-apoptotic signalling was impaired (Figure 6D). Furthermore, KPP, when  
740 compared to KP, deregulated cell cycle checkpoint proteins, apoptosis, mRNA  
741 splicing and chromatid cohesion differentially to KP cells, thereby contributing to the  
742 increased tolerance towards ionizing radiation (Figure S6B). Addition of the small  
743 molecule ATM inhibitor KU-60019, reverted the 'underrepresentation' of  
744 phosphorylation of these factors and restored a pro-apoptotic signature in KPP to the  
745 same extend than KP (Figure 6D). The combination of IR and KU-60019 led to an  
746 increase in the phosphorylation of apoptotic execution phase proteins, apoptosis  
747 induced cleavage of proteins, cell cycle and death receptor signalling (Figure S6B).

748

749 To investigate if these effects indeed affect KP and KPP survival upon the  
750 combination of ionizing radiation and KU-60019, we performed fluorescent activated  
751 cell sorting (FACS) by using DAPI and the apoptosis marker Annexin V (Figure 6E).  
752 Exposure to 8 Gy ionizing radiation or the exposure to 3  $\mu$ M KU-60019 had little  
753 effect on overall cell viability of KP or KPP cells (Figure 6E). Upon exposure to 8 Gy  
754 in combination with 3 $\mu$ M KU-60019, KP cells increased the percentage of cells in the  
755 apoptotic stage (to 30% Annexin V+/DAPI-, Figure 6E and S6C, D). KPP cells were  
756 more sensitive to the combinatorial treatment and showed a marked increase in  
757 apoptotic cells after 96 h, exceeding KP cells (>40% Annexin V+/DAPI-, Figure 6E  
758 and S6C, D).

759

760 These data demonstrate that ionizing radiation resistant *PTEN*<sup>mutant</sup> cells are  
761 addicted to the DNA damage kinase ATM, and ATR nor DNA-PK can substitute for  
762 ATM during therapy. This tumor bottleneck can be exploited, as wild type nor tumor  
763 cells relied on active ATM for cell proliferation, at least *ex vivo*, and tolerated ATM  
764 inhibition via KU-60019 or AZD 1390, while in combination with ionizing radiation  
765 *PTEN*<sup>mutant</sup> cells, human and murine, succumbed to therapy.

766

767 ***Combining ionizing radiation with ATM inhibition results in *PTEN*<sup>mutant</sup> tumor***  
768 ***regression in ex vivo organotypic lung tumor slice cultures***

769

770 The *in vitro* result was reproduced in a multicellular *ex vivo* organotypic lung system  
771 (Figure 7A and Figure S7A). Isogenic murine KP6 and KPP4 cells were  
772 orthotopically re-transplanted in immune-competent C57BL6/J mice (Figure 7A). 8  
773 weeks post-transplantation, mice were sacrificed, and lungs analysed for tumor  
774 engraftment of green fluorescent protein positive (GFP<sup>+</sup>) tumor cells, followed by live  
775 tissue sectioning with a Leica V1200S vibratome and subsequent culture of life  
776 tissue sections in a 24 well plate (Figure 7A). Slices containing tumor (GFP<sup>+</sup>) and  
777 wild type tissue (GFP<sup>-</sup>) were cultured in standard medium (DMEM, 10 % FCS) and  
778 exposed to either IR (8 Gy), 3  $\mu$ M KU-60019, or a combination of both, according to  
779 treatment regime, followed by imaging of GFP<sup>+</sup> cells for indicated time points (Figure  
780 7A and S7A and B). We used the GFP signal of the transplanted tumor cells as a  
781 surrogate marker for cell viability, as dead cells lose GFP signal.

782 Culture of organotypic slices for 8 days showed no deterioration of the GFP signal of  
783 untreated KP and KPP tumor cells (Figure 7B and S7B). Exposure to 3  $\mu$ M KU-  
784 60019 alone did not result in tumor cell death, as seen by consistent GFP intensity  
785 over the course of the experiment (Figure 7B). Exposure of KP transplant tumors to  
786 a single dose of IR (8 Gy) resulted in a reduction in overall GFP signal intensity,  
787 indicating that tumor cells died upon treatment, (Figure 7C). This effect was further  
788 enhanced by combining IR with 3  $\mu$ M KU-60019 (Figure 7C and S7B). Exposure of  
789 KPP transplant tumors to IR alone showed no regression of GFP signal intensity,  
790 thereby confirming the therapy resistance of *PTEN*<sup>mutant</sup> cells in a multicellular  
791 system (Figure 7C and S7B). Combined treatment with 8 Gy and 3  $\mu$ M KU-60019 led

792 to a rapid decrease of the GFP signal in the *PTEN*<sup>mutant</sup> KPP tumors, that rapidly  
793 diminished comparable to *PTEN*<sup>wt</sup> (Figure 7C and S7B).

794

795 These data show that ATM inhibition potentiated IR therapy responses in tumor cells  
796 and re-establishes a sensitivity of otherwise radiation resistant *PTEN*<sup>mutant</sup> tumor  
797 cells. highlighting that targeting ATM could result in a general improvement of IR-  
798 based therapy.

799

## 800 Discussion

801 Radiotherapy is an important modality in cancer treatment. Ionizing radiation inflicts  
802 DNA damage and challenges the complex DNA damage repair machinery in cells.

803 Current knowledge identifies a complex network of more than 800 genes involved in  
804 damage recognition and handling, related cell cycle response and eventually  
805 removal of critically damaged cells. This network is characterized by redundancy and  
806 alternative and fallback pathways (e.g. repair of double strand breaks). From an  
807 evolutionary point of view this is of importance to maintain genomic stability and  
808 control of proliferation in multicellular organisms.

809 Tumor cells, in contrast to non-transformed cells, frequently harbor mutations in  
810 check point genes and fail to halt the cell cycle to initiate the repair of damaged  
811 DNA<sup>50-53</sup>. Mutations in oncogenes, such as *KRAS*<sup>54</sup>, and subsets of loss-of-function  
812 mutations in tumor suppressors, such as *FBXW7*<sup>44, 55</sup> or *STK11*<sup>56</sup>, can cause  
813 resistance to DNA damage based therapies. Identification of exploitable 'bottlenecks'  
814 for tumor cell survival might be an option to advance our current treatment options.

815

816 One such exploitable bottleneck is presented by mutations in the phosphatase and  
817 tensin homologue (*PTEN*). Our analysis of publicly available datasets revealed that  
818 *PTEN* is frequently mutated in NSCLC, ranging from transcriptional downregulation  
819 to genetic loss, and frequently co-occur with gain of function mutations in the  
820 oncogene *KRAS* and loss of function mutations in the tumor suppressor *TP53*. *PTEN*  
821 gene dosage is a direct prognostic marker for therapy outcome and patient survival,  
822 as already a reduction in gene expression negatively correlated with patient survival  
823 and ionizing radiation therapy success for both NSCLC entities, adenocarcinoma  
824 and squamous cell carcinoma. This effect is not limited to NSCLC, but was reported  
825 in other tumor entities where *PTEN* was mutated e.g. glioblastoma and prostate  
826 tumors<sup>57</sup>. Genetic loss accelerates tumor growth, enhances tumor burden and  
827 shortens overall survival<sup>58</sup>.

828 Several murine *in vivo* systems were established to analyse the role of Pten in  
829 cancer progression and survival, such as pancreas<sup>59, 60</sup>, breast<sup>61</sup>, endometrium<sup>62</sup> and  
830 lung<sup>63</sup>. We have established a novel mouse model using CRISPR gene editing to  
831 delete common tumor suppressors, such as *Trp53* and *Pten*, together with mutating  
832 *KRas* to *Kras*<sup>G12D</sup>, to establish primary tumors and cell lines. In this model, we  
833 reproduced both accelerated tumor growth and reduced survival caused after loss of  
834 *Pten*. This genetic alteration was sufficient also to enhance resistance towards  
835 ionizing radiation.

836 Analysis of *PTEN* dependent changes of the transcriptome in our primary murine  
837 lung tumor cells revealed that loss of Pten had a significant impact on gene  
838 expression. Gene sets associated with epithelial–mesenchymal transition (EMT) and  
839 metastasis were enriched together with increased expression of Myc target gene  
840 signatures as well as G2M checkpoint genes and E2F pathway members. Depletion  
841 of Pten also altered the expression of gene sets associated with therapy response, in  
842 particular against ionizing irradiation or doxorubicin treatment, both treatments  
843 causing double strand breaks and ROS<sup>64, 65</sup>. Loss of PTEN obviously profoundly  
844 changes the cellular environment if DNA damage is encountered.

845 Although handling of DNA-damage occurs in a complex and pleiotropic network,  
846 selective gene editing of PTEN using CRISPR/Cas technology led to modification of  
847 radiation sensitivity for a multitude of endpoints (clonogenic survival, cell number and  
848 apoptosis in cell culture and cell viability and tumor size in organ culture). The effect  
849 was found both in a presumable stable “normal” cell line (BEAS-2B) and in a “tumor”  
850 cell line harbouring additional mutations (KP; e.g. p53 and KRas). The specificity of  
851 the intervention was confirmed by reconstitution of PTEN function in the mutated  
852 clones via lentiviral transduction. A reversal of the effects on radiosensitivity was  
853 demonstrated.

854 In BEAS-2B cells, CRISPR gene editing reduced radiation sensitivity in  
855 *PTEN*<sup>heterozygous</sup> and in *PTEN*<sup>homozygous</sup> deficient cells. Our data suggest that IR  
856 resistance strongly correlates with PTEN gene and protein status. Our work also  
857 demonstrated that *PTEN* loss alone is sufficient to drive IR resistance, as the *in*  
858 *cellulo* gene modification in BEAS-2B allowed us to not only create *PTEN*<sup>heterozygous</sup>  
859 and *PTEN*<sup>homozygous</sup> mutant cells, but also to combine it with oncogenic drivers, such  
860 as *BRAF*<sup>V600E</sup>. In our experiments the overexpression of *BRAF*<sup>V600E</sup> had no effect on  
861 IR resistance in BEAS-2B wild type or *PTEN*<sup>mut</sup> single and compound cells, showing  
862 that MAPK pathway alteration has only low impact on radiation sensitivity in this cell  
863 system.

864 Loss of PTEN causes hyper-activation of pAKT and its downstream signals<sup>66</sup>. pAKT,  
865 apart from many other effects, activates DNA-PK, an important protein in the DNA  
866 damage repair cascade, especially in classical non homologous end joining (NHEJ).  
867 We used PI-103 to inhibit the PI3K pathway. However, *PTEN*<sup>mut</sup> cells still showed  
868 lower sensitization to radiation treatment than their *PTEN*<sup>wt</sup> counterpart. This was  
869 potentially due to a fast rebound of pAKT. Alternatively, backup pathways regulating  
870 DNA damage repair might be preferentially active in *PTEN*<sup>mut</sup> cells.

871  
872 Non-transformed and oncogenic transformed cells rely on an efficient mechanism to  
873 identify and repair damaged DNA. The major DNA kinases, DNA-PK<sup>66</sup>, ATR<sup>67</sup> and  
874 ATM<sup>68</sup>, recognize various types of damage, ranging from interstrand crosslink to  
875 single- and double strand breaks, and initiate downstream repair pathways, such as  
876 non-homologous end joining or homologous repair<sup>69</sup>.

877 In mammalian cells NHEJ is the dominant way of repairing DNA-double strand  
878 breaks. This constitutes a fast, partly error prone mechanism. Recent data show that  
879 fidelity and effectiveness of NHEJ depends on the extent of microhomology and

880 overlaps with a further DNA-PK independent repair pathway (alternative-end joining).  
881 Interestingly, inhibition of DNA-PK via the compound PI-103 had no effect on IR  
882 resistance of KP nor KPP cells and only marginally induced IR sensitivity in  
883 BEAS-2B single and compound mutant cells.

884 So called toxic non-homologous end joining has been identified in ATM-deficient  
885 models if ATR was inhibited. We discuss a similar scenario in our models, where in  
886 PTEN deficient cells IR failed to elicit ATR activation as backup repair pathway, and  
887 subsequent ATM-inhibition caused strong radio sensitization.

888 The failure to activate ATR upon exposure to ionizing radiation was unexpected.  
889 However, PTEN is a key signal transducer and has functions independent of its  
890 proliferation directed cytoplasmic lipid phosphatase activity. Recent studies suggest  
891 that PTEN also localizes in the nucleus and is involved in chromatin functions<sup>70</sup>. Ma  
892 et al. showed that phosphorylation of PTEN at tyrosine 240 enhanced DDR via  
893 Rad51 and homologous end joining repair<sup>71</sup>.

894 Hence, we assume that KPP and BEAS-2B PTEN<sup>mut</sup> with loss of PTEN function,  
895 mainly relied on ATM and NHEJ to sense and resolve DNA damage after irradiation.  
896 Treatment with ATM-inhibitors KU-60019 and AZD 1390 in low concentrations had  
897 no effect on cell survival or proliferation of Pten mutant and wild type cells. However,  
898 in combination with ionizing radiation it enhanced radiation sensitivity  
899 disproportionately in PTEN<sup>mut</sup> and abolished the difference to the wild type. This  
900 effect was demonstrated both in classical cell culture and in an organotypic  
901 multicellular system. The combined treatment of PTEN<sup>mut</sup> NSCLC by IR and ATM  
902 inhibition led to marked tumor regression.

903

904 This combination is synergistic and seems especially active in PTEN deficient  
905 tumors. While ATM inhibitors can be given with low systemic side effects, modern  
906 radiotherapy localizes treatment to the tumor with tight margins. This could create  
907 "spatial cooperation" in otherwise relatively radiation resistant tumors. A first clinical  
908 trial is evaluating tolerance of ATM inhibitors and radiation therapy (NCT03423628).  
909 The trial does not stratify treatment for different genetic backgrounds and therefore  
910 could miss significant improvement for selected but common groups, like patients  
911 with PTEN deficient tumors. We suggest that genetic stratification and personalized  
912 treatment might gain importance also in radiation therapy. PTEN and ATM are  
913 already part of clinically established tumor sequencing panels and results should find  
914 access to therapeutic decisions.

915

## 916 **Conclusion**

917 In this study, we investigated the role of PTEN in response to radiation induced  
918 damage by genetically modulating PTEN in the human tracheal stem cell like cell line  
919 BEAS-2B. We observed in compound mutant cell lines that the IR resistance  
920 phenotype of PTEN-deficient tumors is indeed dictated by alterations in PTEN alone.  
921 This was validated in murine models of NSCLC, where loss of Pten induced IR  
922 resistance as well. The effect was not resolved by inhibition of DNA-PK and  
923 independent of ATR activation. However, pharmacological ATM inhibition (via the

924 small molecules KU-60019 or AZD 1390) was able to increase radiation sensitivity  
925 and pointed to a crucial role of the DNA damage kinase ATM in a PTEN-deficient  
926 situation. These results from monolayer cell culture were reproduced *in* and *ex vivo*  
927 organotypic slice culture assay. Analysis of transcriptional changes upon PTEN  
928 loss and obvious differences in activation of  $\gamma$ H2AX points to shifts in DNA damage  
929 detection and response and resulting synthetic lethality in PTEN-deficient tumors.  
930 Our study suggests that tumors harbouring a loss of function mutation in PTEN can  
931 be therapeutically addressed by irradiation in combination with ATM inhibition.

932

### 933 **Abbreviations**

934	<b>DMSO</b>	dimethyl sulfoxide
935	<b>RER</b>	radiation enhancement ratio
936	<b>DER</b>	dose enhancement ratio
937	<b>KP</b>	<i>KRas<sup>G12D</sup>:Tp53<sup>mut</sup></i>
938	<b>KPP</b>	<i>KRas<sup>G12D</sup>:Tp53<sup>mut</sup>.Pten<sup>mut</sup></i>
939	<b>H&amp;E</b>	haematoxylin and eosin
940	<b>NSCLC</b>	non-small cell lung cancer
941	<b>UICC</b>	union internationale contre le cancer
942	<b>NGS</b>	next generation sequencing
943	<b>PTEN</b>	phosphatase and tensin homologue
944	<b>ROS</b>	reactive oxygen species
945	<b>UICC</b>	union internationale contre le cancer
946	<b>IR</b>	ionizing radiation
947	<b>ATM</b>	ataxia telangiectasia mutated kinase
948	<b>ADC</b>	adenocarcinoma
949	<b>SCC</b>	squamous cell carcinoma
950	<b>TMB</b>	tumor mutational burden
951	<b>AAV</b>	adeno-associated virus
952	<b>GSEA</b>	gene set enrichment analysis
953	<b>DDR</b>	DNA damage response
954	<b>FACS</b>	fluorescent activated cell sorting
955	<b>GFP</b>	green fluorescent protein
956	<b>NHEJ</b>	homologous end joining

957

### 958 **Acknowledgements**

959 We are grateful to the animal facility and Barbara Bauer at the Biocenter, University  
960 Würzburg. We thank Clare C. Davies from University of Birmingham for critical  
961 suggestions and discussions. C.P.G. and O.H. are supported by the German Cancer  
962 Aid via grant 70112491, M.R. is funded by the DFG-GRK 2243 and IZKF B335.  
963 M.E.D. and M.R. are funded by the German Israeli Foundation grant 1431. T. F. is  
964 funded by the IZKF program Z2/CS-1.

965

### 966 **Author contributions**

967 Conceptualization: T.F., M.E.D.; Methodology: T.F. (in vitro) and O.H. (*in vivo*),  
968 C.S.V. (Operetta system); Formal analysis: C.P.G. and M.Re. (Bioinformatics),  
969 M.Ro. and M.E.D. (Pathology); Investigation: T.F., O.H., M.Re., C.P.G. B.P. M.Ro.,  
970 M.E.D. Resources: M.Ro., M.F., M.E.D.; Writing-original draft: M.E.D.; Writing-review  
971 and editing: T.F., O.H., M.Re., M.Ro, M.F., M.E.D.; Supervision: M.E.D.; Funding  
972 acquisition: T.F., M.F., M.E.D.

973

974 **Conflict of Interest:**

975 The authors declare no potential conflicts of interest.

976

977

978

979

980

981

982

983

984

985

986

987

988

989

990

991

992

993

994

995

996

997

998

999

1000

1001

1002

1003

1004

1005

1006

1007

1008

1009

1010



1011  
1012  
1013  
1014  
1015  
1016  
1017

## 1018 **FIGURE LEGENDS**

1019  
1020  
1021  
1022  
1023  
1024  
1025  
1026  
1027  
1028  
1029  
1030  
1031  
1032  
1033  
1034  
1035  
1036  
1037  
1038  
1039  
1040  
1041  
1042  
1043  
1044  
1045

Figure 1: PTEN alterations; impact on pathways and radiation resistance

- A) PTEN alteration frequency of NSCLC from cBioportal, <https://www.cbioportal.org/>. Analysis of Lung Squamous Cell Carcinoma (SCC) and Adenocarcinoma (ADC).
- B) Kaplan-Meier Plot of lung cancer patient survival stratified by PTEN (204054\_at) expression. Median survival in the ADC cohort of the low PTEN expression 61.3 months, of high expression 175 months. Median survival in the SCC cohort of the low PTEN expression 42 months, of high expression 72.3 months. The p-value was calculated using a logrank test. HR: hazard ratio. Generated with the online tool <https://kmplot.com>.
- C) Schematic representation of the CRISPR/Cas9 genome editing strategy to delete PTEN in the human lung cell line BEAS-2B targeting exon 1 and exon 4.
- D) Immunoblot of virus transfected, blasticidin selected and clonogenic isolated BEAS-2B cells, generated with the described method (Supp. Figure 2B). Control: WT: Epithelial transformed BEAS-2B PTEN<sup>wt</sup> cells. Actin as loading control.
- E) Receptor-tyrosine-kinase signaling cascade of the MAPK-pathway and PI3K/Akt pathway. Numbers next to the Enzymes show the percentage of genetic alteration of the coding genes. Data generated with the free online tool [www.cbioportal.org](http://www.cbioportal.org).
- F) Colony formation assay BEAS-2B clone II1 (PTEN<sup>hetero</sup>, light blue) and III3 (PTEN<sup>homo</sup>, blue) compared to vector control (black). SF 2: Surviving fraction at 2 Gy. D<sub>25</sub>: Dose in Gy with 25% survival. Error bars: Standard deviation. n=3.

1046 Also see Supplementary Figure S1.

1047  
1048  
1049  
1050  
1051  
1052  
1053  
1054  
1055  
1056  
1057  
1058

Figure 2: Generating and characterizing murine PTEN deficient tumor cell lines

- A) Representative haematoxylin and eosin (H&E) staining of tumor bearing animals 12 weeks post intratracheal infection. On the left KP ( $KRas^{G12D}:Tp53^{mut}$ ) on the right KPP ( $KRas^{G12D}:Tp53^{mut}:Pten^{mut}$ ). Boxes indicate upper highlighted tumor areas.
- B) Representative haematoxylin and eosin (H&E) and immunohistochemical DAB staining (PTEN, p-ERK1/2 and p-S6) of tumor bearing animals 12 weeks post intratracheal infection. on the upper part KP ( $KRas^{G12D}:Tp53^{mut}$ ) on the lower part KPP ( $KRas^{G12D}:Tp53^{mut}:Pten^{mut}$ ).
- C) Quantification of % tumor area (normalized to total lung area) in KP (black) and KPP (blue) animals. n=3.

- 1059 D) Kaplan-Meier survival curves comparing KP (black; n=5) and KPP (blue,  
1060 n=5) animals upon AAV intratracheal infection.  
1061 E) Immunoblot of endogenous (phospho-)AKT of two representative  
1062 generated cell lines from different mice. KP5 and KP6 ( $KRas^{G12D}:Tp53^{mut}$ ),  
1063 KPP4 and KPP8 ( $KRas^{G12D}:Tp53^{mut}:Pten^{mut}$ ). Actin as loading control. n=3.  
1064 F) Colony formation assay KP5 (gray), KP6 (black), KPP4 (blue) and KPP8  
1065 (light blue). SF 2: Surviving fraction at 2 Gy. D<sub>25</sub>: Dose in Gy with 25%  
1066 survival. Error bars: Standard deviation. n=3.  
1067 G) Immunoblot against PTEN/Pten of KP6 and lentivirally transduced, either  
1068 GFP or human PTEN cDNA overexpressing KPP4 cells after Puromycin  
1069 selection. Actin as loading control. n=3.  
1070 H) Colony formation assay KPP4 (blue) and PTEN reconstituted KPP4 clones  
1071 (C5, C7, C15 and C18; gray to black; Supp. Figure 3D) after clonogenic  
1072 isolation. SF 2: Surviving fraction at 2 Gy. D<sub>25</sub>: Dose in Gy with 25%  
1073 survival. Error bars: Standard deviation. n=3.  
1074

1075 Also see Supplementary Figure S2.

1076

1077 Figure 3: Loss of *Pten* alters DNA damage signalling pathways in murine NSCLC

- 1078 A) Correlation of gene expression changes of  $KRas^{G12D}:Trp53$  (KP6) relative  
1079 to  $KRas^{G12D}:Trp53:Pten$  (KPP4). The diagonal line reflects a regression  
1080 build on a linear model. R: Pearsons correlation coefficient. R=0.9122.  
1081 B) Venn diagram of differentially up-regulated genes ( $\log_2FC>1.0$  and q-  
1082 value<0.05) between  $KRas^{G12D}:Trp53$  (KP6) relative to  
1083  $KRas^{G12D}:Trp53:Pten$  (KPP4).  
1084 C) Volcano blot of differentially up- and downregulated genes in  
1085  $KRas^{G12D}:Trp53:Pten$  (KPP4) relative to  $KRas^{G12D}:Trp53$  (KP6).  $\log_2FC$  cut-  
1086 off >1.0,  $-\log_{10}FC >1.5$ . Highlighted are genes involved in IR resistance;  
1087 *SftpC*, *Slc34a2*, *Tub*, *Myh6* and *Shh*, or IR sensitivity, *Wisp2* and *Bex1*.  
1088 n=3  
1089 D) Gene set enrichment analysis (GSEA) of Gamma radiation response,  
1090 doxorubicin resistance up, KRas targets up, AKT1 signaling via mTOR,  
1091 mesenchymal transition and metastasis  $KRas^{G12D}:Trp53$  (KP) relative to  
1092  $KRas^{G12D}:Trp53:Pten$  (KPP). n=3 each. Table with normalized enrichment  
1093 score ((N)ES) and p-Value of GSEA.  
1094

1095 Also see Supplementary Figure S3.

1096

1097 Figure 4: Impact of PI3K/mTOR inhibition in PTEN deficient cells

- 1098 A) Representative Immunoblot of KP6 and KPP4 cells without and with 2 $\mu$ M  
1099 PI-103 treatment 3h before irradiation with 8 Gy at time points directly, 2h,  
1100 4h, 8h and 24h after irradiation. DMSO as solvent control. Actin and AKT  
1101 as loading control. n=3.  
1102 B) Colony formation assay KP6 (black) and KPP4 (blue) cells with 2  $\mu$ M PI-  
1103 103 (dashed lines) and DMSO as control (continuous lines) with re-  
1104 seeding protocol (Figure S4A). SF 2: Surviving fraction at 2 Gy. D<sub>25</sub>: Dose  
1105 in Gy with 25% survival. Error bars: Standard deviation. n=3.  
1106 C) Relative number of living of KP6 (black) and KPP4 (blue) cells 27h after  
1107 treatment with PI-103 in different concentrations, DMSO as control and 24

- 1108 h after radiation with 8 Gy (dashed lines) or without radiation (continuous  
1109 lines) (dead cells stained with trypan blue excluded from analysis). Error  
1110 bars: Standard deviation. n=3.  
1111 D) Immunoblot of (phospho-)AKT and (phospho-)S6 BEAS-2B wildtype (WT),  
1112 *PTEN<sup>homo</sup>*, *BRAF<sup>V600E</sup>* and compound mutant cell lines without and with  
1113 2  $\mu$ M PI-103 pre-treatment for 3 h. DMSO as solvent control. Actin serves  
1114 as loading control.  
1115 E) Colony formation assay of WT (black) and PTEN deficient (blue) BEAS-2B  
1116 cells with 3 h pre-treatment of 2  $\mu$ M PI-103 (dashed lines) and DMSO as  
1117 control (continuous lines) with 24 h re-seeding protocol (Figure S4A). SF  
1118 2: Surviving fraction at 2 Gy. D<sub>25</sub>: Dose in Gy with 25% survival. Error  
1119 bars: Standard deviation. n=3.  
1120

1121 Also see Supplementary Figure S4.

1122

1123 Figure 5: Impact of ATM inhibition in PTEN deficient cells

- 1124 A) Dose response of BEAS-2B WT (black) and BEAS-2B *PTEN<sup>homo</sup>* (blue)  
1125 BEAS-2B cells on colony forming ability following treatment with KU-60019  
1126 in different concentrations. Error bars: Standard deviation. n=3.  
1127 B) Dose response of murine PTEN proficient KP6 (black) and PTEN deficient  
1128 KPP4 cells on colony forming ability following treatment with KU-60019 in  
1129 different concentrations. Error bars: Standard deviation. n=3.  
1130 C) Immunoblot of WT and PTEN deficient BEAS-2B cells 30 min after  
1131 irradiation with 8 Gy and 3 h pre-treatment with 0,3  $\mu$ M and 3  $\mu$ M KU-  
1132 60019 before irradiation. DMSO as solvent control. Actin, ATM and AKT  
1133 as loading control. n=3.  
1134 D) Immunoblot of murine PTEN proficient KP6 and PTEN deficient KPP4  
1135 cells 30 min after irradiation with 8 Gy and 3 h pre-treatment with 0,3  $\mu$ M  
1136 and 3  $\mu$ M KU-60019 before irradiation. DMSO as solvent control. Actin,  
1137 ATM and AKT as loading control. n=3.  
1138 E) Colony formation assay of WT (black) and PTEN deficient (blue) BEAS-2B  
1139 cells with 3 h pre-treatment of 3  $\mu$ M KU-60019 (dashed lines) and DMSO  
1140 as control (continuous lines) with 24 h re-seeding protocol (Figure S4A).  
1141 SF 2: Surviving fraction at 2 Gy. D<sub>25</sub>: Dose in Gy with 25% survival. Error  
1142 bars: Standard deviation. n=3.  
1143 F) Colony formation assay of murine PTEN proficient KP6 (black) and PTEN  
1144 deficient KPP4 cells with 3 h pre-treatment 3  $\mu$ M KU-60019 (dashed lines)  
1145 and DMSO as control (continuous lines) with re-seeding protocol (Figure  
1146 S4A). SF 2: Surviving fraction at 2 Gy. D<sub>25</sub>: Dose in Gy with 25% survival.  
1147 Error bars: Standard deviation. n=3.  
1148

1149 Also see Supplementary Figure S5.

1150

1151 Figure 6: Multilevel proteomics show differential apoptosis signaling

- 1152 A) Heatmap of KP and KPP phosphorylation sites after treatment with solvent  
1153 control, KU-60019, radiation and combined treatment. Phosphosites  
1154 (rows) and samples (columns) have been hierarchically clustered using  
1155 Euclidean distance. Quantification values have been standardized using Z-  
1156 scoring to account for different scales. Color scales indicate Z-scores.

- 1157 B) Enrichment map showing Reactome pathways differentially regulated  
1158 (log<sub>2</sub> fold change differences >0.5) between KP and KPP cells upon  
1159 radiation. Related pathways are connected by edges. Node coloring  
1160 corresponds to ReactomeFI functional enrichment score. All pathways  
1161 shown are significantly enriched with an FDR < 0.05.  
1162 C) Heatmap showing total protein fold changes of apoptosis hallmark genes  
1163 upon radiation and combinatorial treatment in KP and KPP cell lines.  
1164 Clustering has been performed using hierarchical clustering with Euclidean  
1165 distance.  
1166 D) Bar graph showing log<sub>2</sub> fold changes for genes identified in cluster I from  
1167 C. The data indicates that combinatorial treatment rescues the expression  
1168 differences upon radiation between the two cell lines.  
1169 E) AnnexinV/DAPI staining of KP6 and KPP4 cells with 3 h pre-treatment  
1170 3 μM KU-60019 and DMSO as control with and without irradiation 8 Gy,  
1171 96h post irradiation. Supernatant of 96 h cultivation Medium was collected  
1172 with trypsinized cells before staining. The lower right quadrant of the dot  
1173 plots shows the apoptotic fraction measured with flow cytometer. The  
1174 diagram shows the apoptotic fraction after 96h with different treatments.  
1175 Error bars: Standard deviation.  
1176

1177 Also see Supplementary Figure S6.

1178  
1179 Figure 7: Tumor slice culture response to KU-60019 treatment and radiation

- 1180 A) Schematic of orthotopic transplantation of GFP positive KP6 and KPP4  
1181 cells to immune competent C57BL/6 mice. The picture shows GFP  
1182 positive tumors in mouse lungs after 8 weeks. The tumor bearing mouse  
1183 lungs were cut by vibratome and cultured in 10% FCS/DMEM in 24 well  
1184 plates. Culture slices were treated with DMSO or ATM inhibitor and  
1185 irradiated with 0 Gy or 8 Gy.  
1186 B) Tissue slices (n=2-4) of transplanted KP6 (black) and KPP4 (blue) were  
1187 pre-treated with DMSO (continuous line) or 3 μM Ku60019 (dashed line)  
1188 Treated tissue slices were observed and pictures of same tumor sites  
1189 were taken for 8 days. The fluorescent signal of the tumor area was  
1190 measured, and background area was subtracted. On the Graphs the GFP  
1191 signal over time with different treatment conditions is shown. Below each  
1192 graph are typical pictures of measured tumor sites illuminated with  
1193 standardized 488 nm led light source and same camera settings.  
1194 C) Tissue slices (n=2-4) of transplanted KP6 (black) and KPP4 (blue) were  
1195 pre-treated with DMSO (continuous line) or 3 μM Ku60019 (dashed line)  
1196 and irradiated with 8 Gy. Treated tissue slices were observed and pictures  
1197 of same tumor sites were taken for 8 days. The fluorescent signal of the  
1198 tumor area was measured, and background area was subtracted. On the  
1199 Graphs the GFP signal over time with different treatment conditions is  
1200 shown. Below each graph are typical pictures of measured tumor sites  
1201 illuminated with standardized 488 nm led light source and same camera  
1202 settings.  
1203

1204 Also see Supplementary Figure S7.

1205  
1206

1207  
1208  
1209  
1210  
1211  
1212  
1213  
1214  
1215

## 1216 **REFERENCES**

1217  
1218  
1219  
1220  
1221  
1222  
1223  
1224  
1225  
1226  
1227  
1228  
1229  
1230  
1231  
1232  
1233  
1234  
1235  
1236  
1237  
1238  
1239  
1240  
1241  
1242  
1243  
1244  
1245  
1246  
1247  
1248  
1249  
1250  
1251  
1252

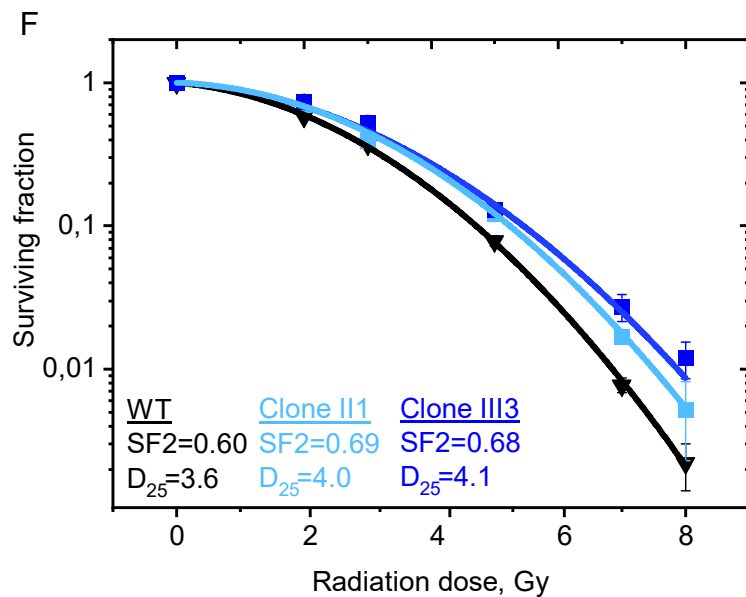
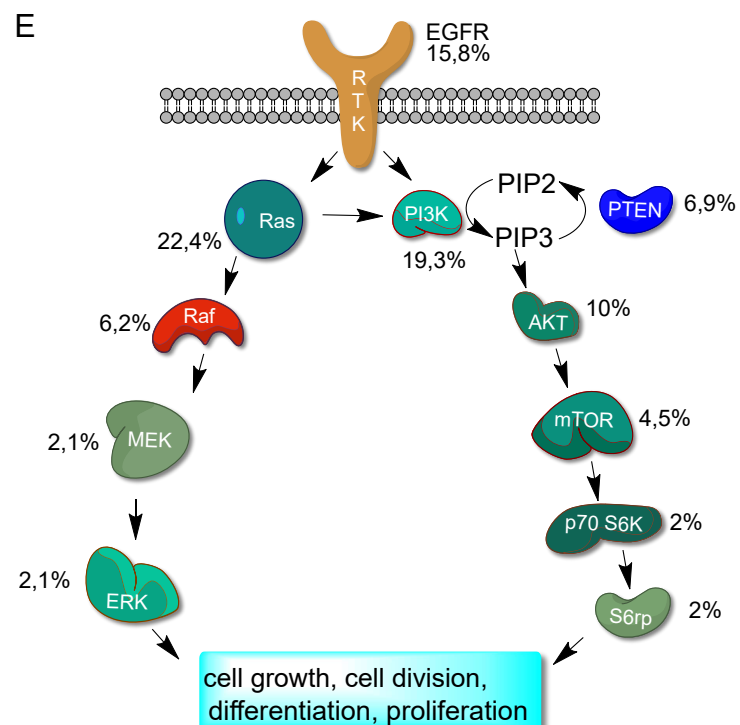
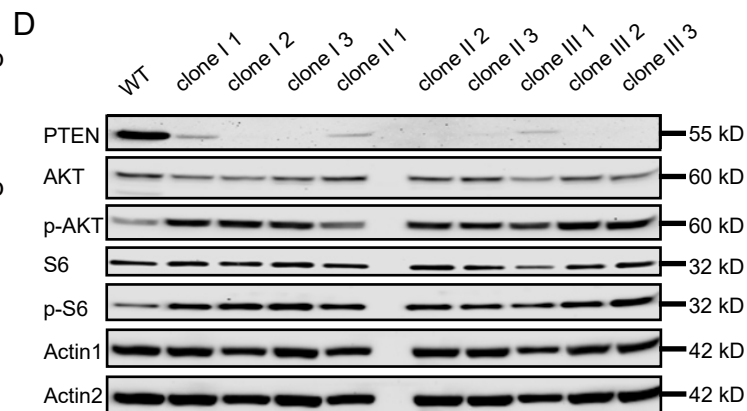
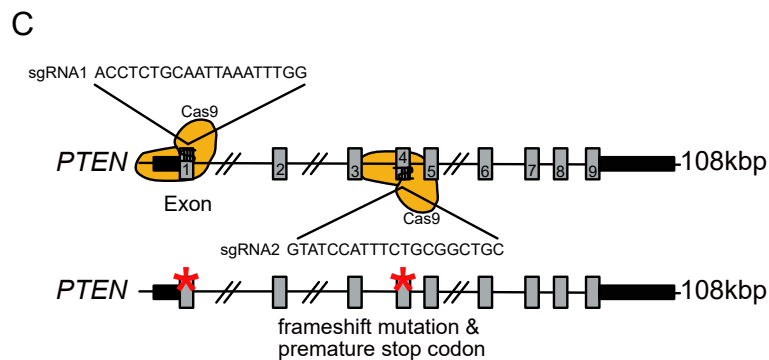
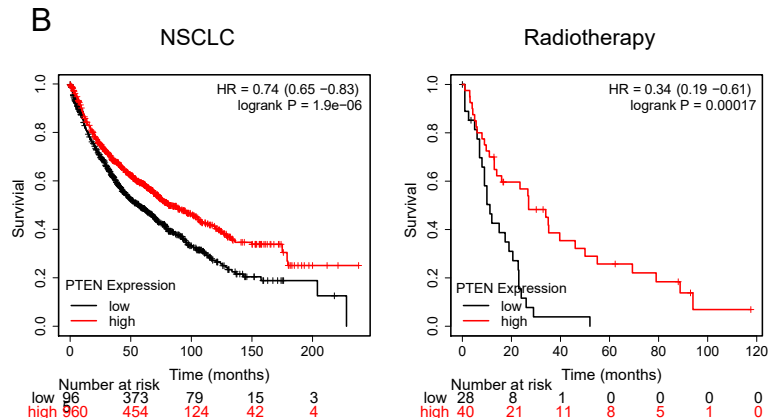
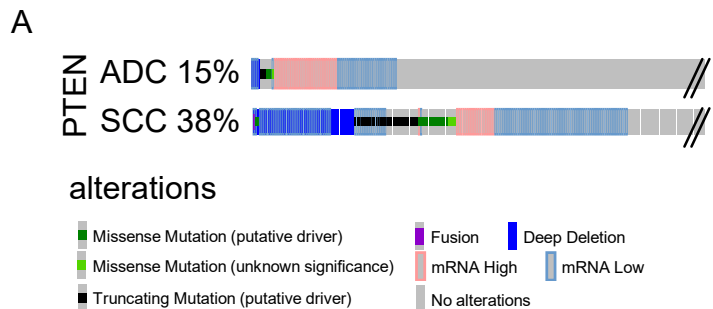
1. Kohlbrenner, E. *et al.* Quantification of AAV particle titers by infrared fluorescence scanning of coomassie-stained sodium dodecyl sulfate-polyacrylamide gels. *Hum Gene Ther Methods* **23**, 198-203 (2012).
2. Buchel, G. *et al.* Association with Aurora-A Controls N-MYC-Dependent Promoter Escape and Pause Release of RNA Polymerase II during the Cell Cycle. *Cell Rep* **21**, 3483-3497 (2017).
3. Kim, D. & Salzberg, S.L. TopHat-Fusion: an algorithm for discovery of novel fusion transcripts. *Genome Biol* **12**, R72 (2011).
4. Langdon, W.B. Performance of genetic programming optimised Bowtie2 on genome comparison and analytic testing (GCAT) benchmarks. *BioData Min* **8**, 1 (2015).
5. Robinson, M.D., McCarthy, D.J. & Smyth, G.K. edgeR: a Bioconductor package for differential expression analysis of digital gene expression data. *Bioinformatics* **26**, 139-140 (2010).
6. Mi, H., Muruganujan, A. & Thomas, P.D. PANTHER in 2013: modeling the evolution of gene function, and other gene attributes, in the context of phylogenetic trees. *Nucleic Acids Res* **41**, D377-386 (2013).
7. Gao, J. *et al.* Integrative analysis of complex cancer genomics and clinical profiles using the cBioPortal. *Sci Signal* **6**, pl1 (2013).
8. Cerami, E. *et al.* The cBio cancer genomics portal: an open platform for exploring multidimensional cancer genomics data. *Cancer Discov* **2**, 401-404 (2012).
9. Nagy, A., Munkacsy, G. & Gyorffy, B. Pancancer survival analysis of cancer hallmark genes. *Sci Rep* **11**, 6047 (2021).
10. McAlister, G.C. *et al.* MultiNotch MS3 enables accurate, sensitive, and multiplexed detection of differential expression across cancer cell line proteomes. *Anal Chem* **86**, 7150-7158 (2014).
11. Ferlay, J. *et al.* Estimating the global cancer incidence and mortality in 2018: GLOBOCAN sources and methods. *Int J Cancer* **144**, 1941-1953 (2019).
12. Cancer Genome Atlas Research, N. *et al.* The Cancer Genome Atlas Pan-Cancer analysis project. *Nat Genet* **45**, 1113-1120 (2013).
13. Cancer Genome Atlas Research, N. Comprehensive molecular profiling of lung adenocarcinoma. *Nature* **511**, 543-550 (2014).
14. Cancer Genome Atlas Research, N. Comprehensive genomic characterization of squamous cell lung cancers. *Nature* **489**, 519-525 (2012).
15. Moreira, A.L. & Eng, J. Personalized therapy for lung cancer. *Chest* **146**, 1649-1657 (2014).

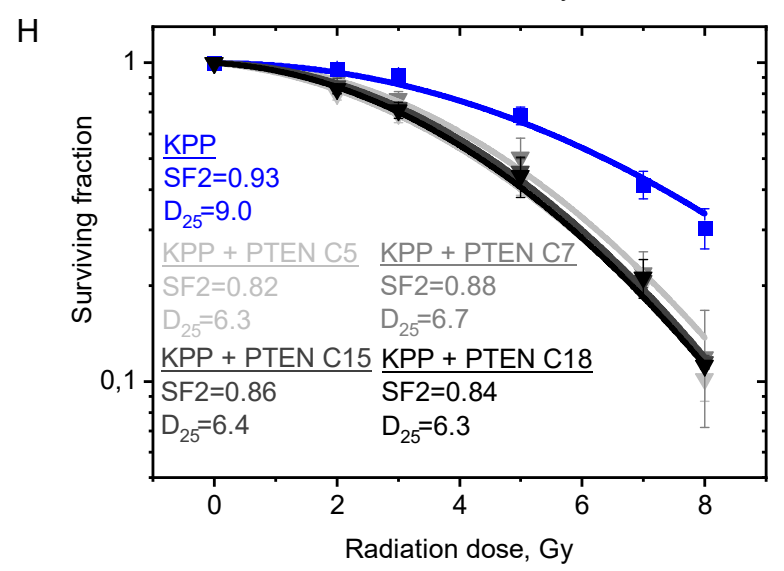
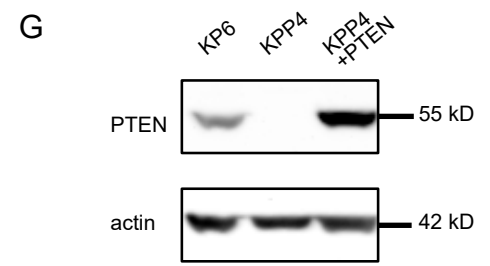
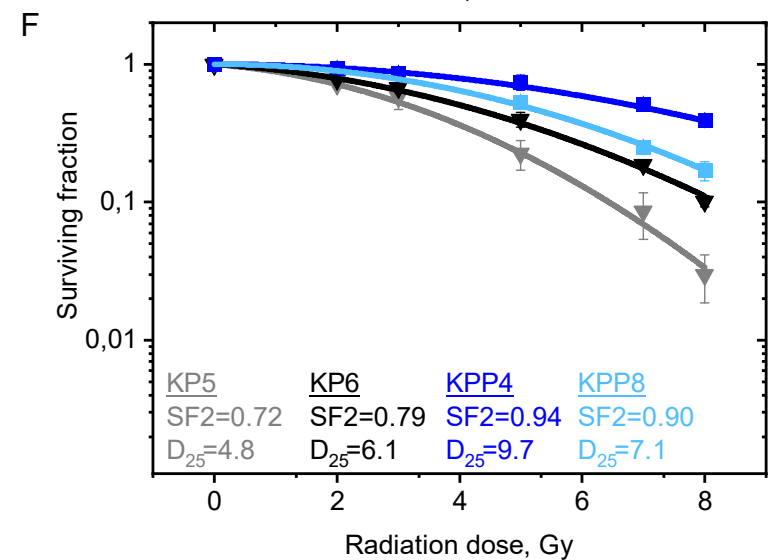
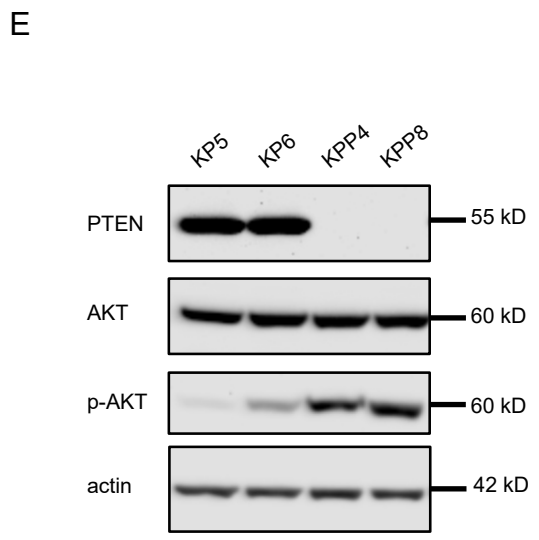
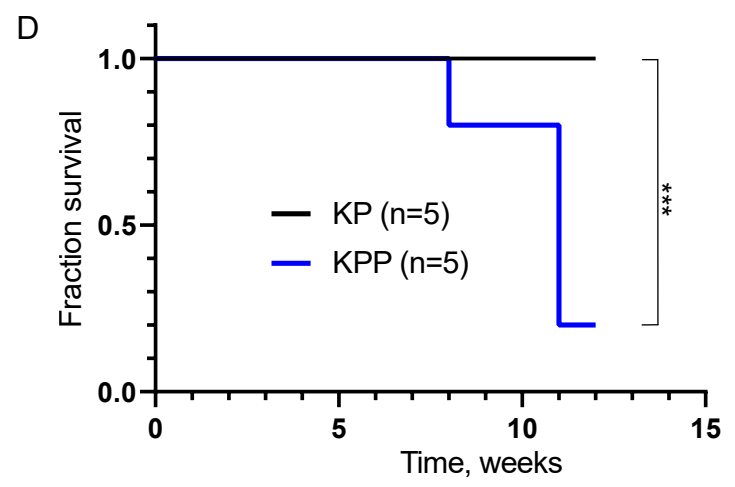
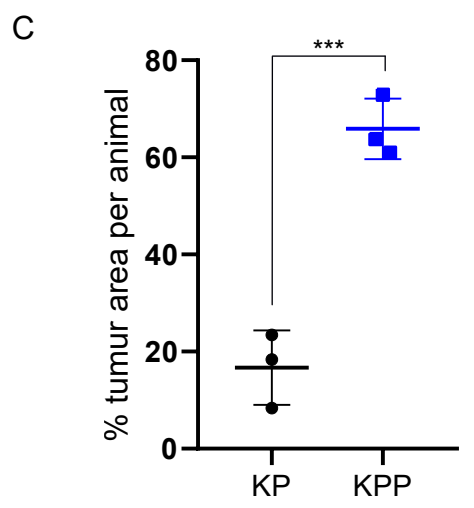
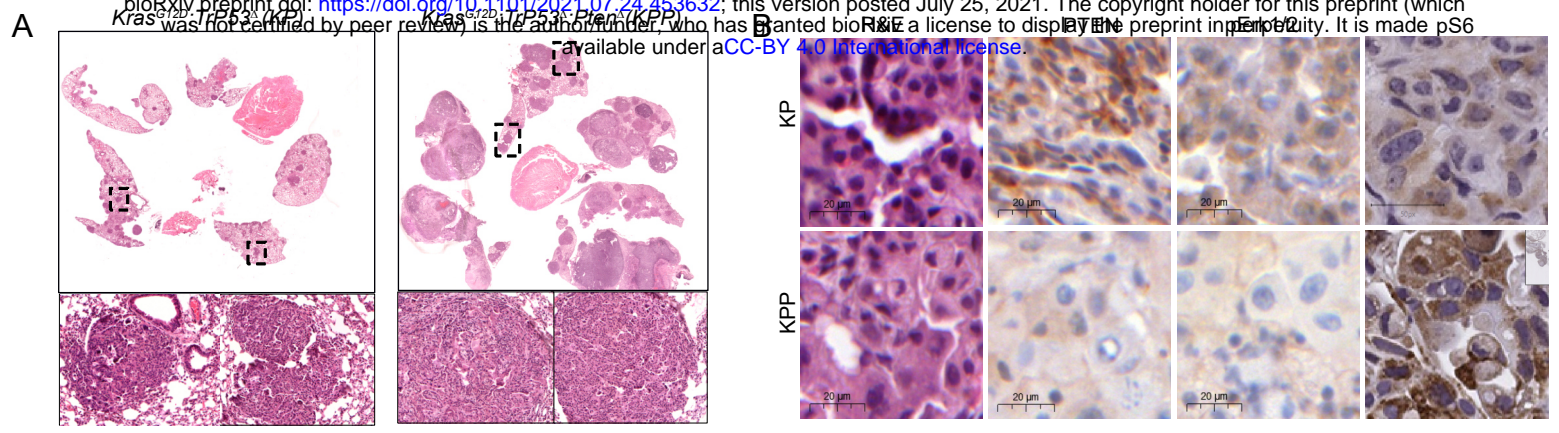
- 1253 16. Pakkala, S. & Ramalingam, S.S. Personalized therapy for lung cancer: striking a  
1254 moving target. *JCI Insight* **3** (2018).
- 1255 17. McDonald, F. *et al.* Management of stage I and II nonsmall cell lung cancer. *Eur*  
1256 *Respir J* **49** (2017).
- 1257 18. Siegel, R.L., Miller, K.D. & Jemal, A. Cancer statistics, 2018. *CA Cancer J Clin* **68**, 7-30  
1258 (2018).
- 1259 19. Varlotto, J.M. *et al.* Failure rates and patterns of recurrence in patients with resected  
1260 N1 non-small-cell lung cancer. *Int J Radiat Oncol Biol Phys* **81**, 353-359 (2011).
- 1261 20. Taugner, J. *et al.* Pattern-of-failure and salvage treatment analysis after  
1262 chemoradiotherapy for inoperable stage III non-small cell lung cancer. *Radiat Oncol*  
1263 **15**, 148 (2020).
- 1264 21. Gajra, A. *et al.* Time-to-Treatment-Failure and Related Outcomes Among 1000+  
1265 Advanced Non-Small Cell Lung Cancer Patients: Comparisons Between Older Versus  
1266 Younger Patients (Alliance A151711). *J Thorac Oncol* **13**, 996-1003 (2018).
- 1267 22. Liu, L. *et al.* PTEN inhibits non-small cell lung cancer cell growth by promoting G0/G1  
1268 arrest and cell apoptosis. *Oncol Lett* **17**, 1333-1340 (2019).
- 1269 23. Hamarshah, S., Gross, O., Brummer, T. & Zeiser, R. Immune modulatory effects of  
1270 oncogenic KRAS in cancer. *Nat Commun* **11**, 5439 (2020).
- 1271 24. Papillon-Cavanagh, S., Doshi, P., Dobrin, R., Szustakowski, J. & Walsh, A.M. STK11  
1272 and KEAP1 mutations as prognostic biomarkers in an observational real-world lung  
1273 adenocarcinoma cohort. *ESMO Open* **5** (2020).
- 1274 25. Chen, C.Y., Chen, J., He, L. & Stiles, B.L. PTEN: Tumor Suppressor and Metabolic  
1275 Regulator. *Front Endocrinol (Lausanne)* **9**, 338 (2018).
- 1276 26. Lee, Y.R., Chen, M. & Pandolfi, P.P. The functions and regulation of the PTEN tumour  
1277 suppressor: new modes and prospects. *Nat Rev Mol Cell Biol* **19**, 547-562 (2018).
- 1278 27. Xiao, J. *et al.* PTEN expression is a prognostic marker for patients with non-small cell  
1279 lung cancer: a systematic review and meta-analysis of the literature. *Oncotarget* **7**,  
1280 57832-57840 (2016).
- 1281 28. Chang, L. *et al.* PI3K/Akt/mTOR pathway inhibitors enhance radiosensitivity in  
1282 radioresistant prostate cancer cells through inducing apoptosis, reducing autophagy,  
1283 suppressing NHEJ and HR repair pathways. *Cell Death Dis* **5**, e1437 (2014).
- 1284 29. Vidotto, T. *et al.* Emerging role of PTEN loss in evasion of the immune response to  
1285 tumours. *Br J Cancer* **122**, 1732-1743 (2020).
- 1286 30. Vivanco, I. *et al.* The phosphatase and tensin homolog regulates epidermal growth  
1287 factor receptor (EGFR) inhibitor response by targeting EGFR for degradation. *Proc*  
1288 *Natl Acad Sci U S A* **107**, 6459-6464 (2010).
- 1289 31. Hou, S.Q., Ouyang, M., Brandmaier, A., Hao, H. & Shen, W.H. PTEN in the  
1290 maintenance of genome integrity: From DNA replication to chromosome  
1291 segregation. *Bioessays* **39** (2017).
- 1292 32. Song, M.S. *et al.* Nuclear PTEN regulates the APC-CDH1 tumor-suppressive complex  
1293 in a phosphatase-independent manner. *Cell* **144**, 187-199 (2011).
- 1294 33. Chen, Z.H. *et al.* PTEN interacts with histone H1 and controls chromatin  
1295 condensation. *Cell Rep* **8**, 2003-2014 (2014).
- 1296 34. Sun, Z. *et al.* PTEN C-terminal deletion causes genomic instability and tumor  
1297 development. *Cell Rep* **6**, 844-854 (2014).
- 1298 35. Furdui, C.M. Ionizing radiation: mechanisms and therapeutics. *Antioxid Redox Signal*  
1299 **21**, 218-220 (2014).

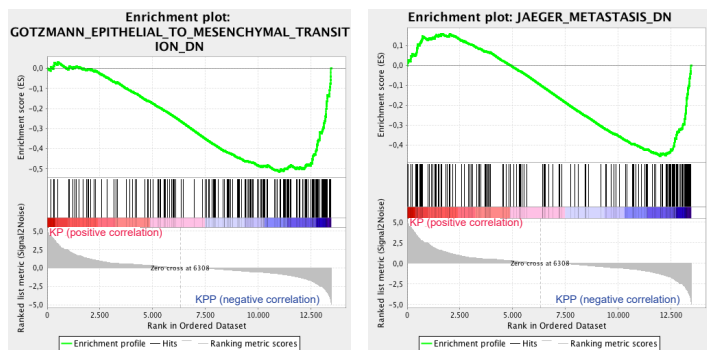
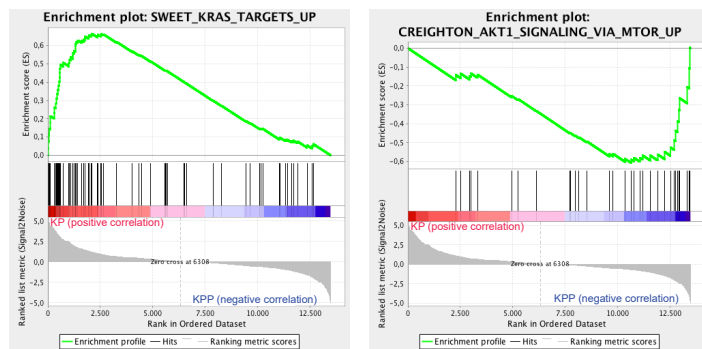
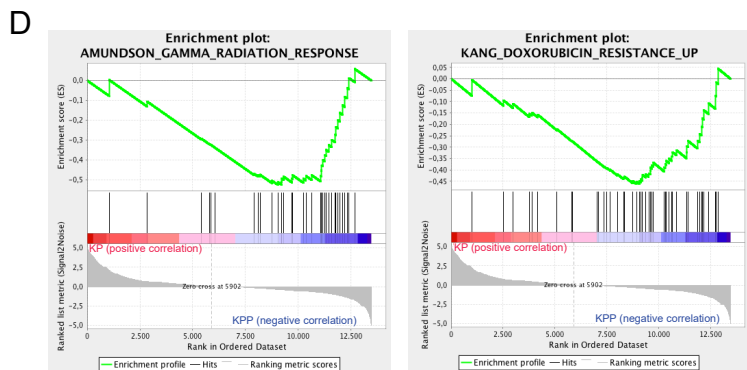
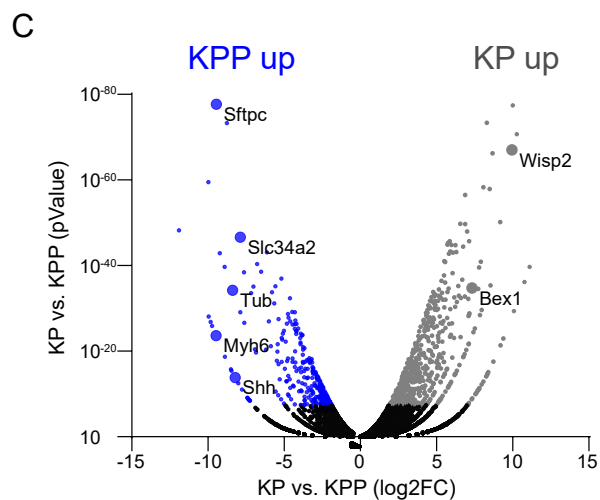
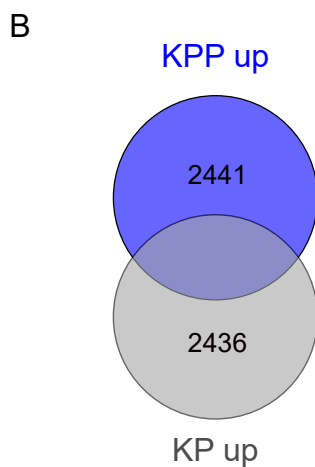
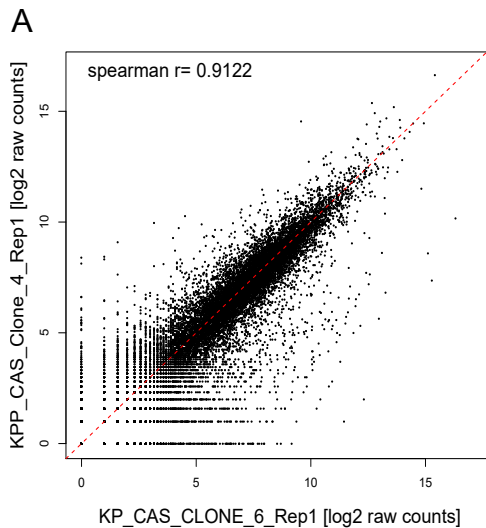
- 1300 36. Borrego-Soto, G., Ortiz-Lopez, R. & Rojas-Martinez, A. Ionizing radiation-induced  
1301 DNA injury and damage detection in patients with breast cancer. *Genet Mol Biol* **38**,  
1302 420-432 (2015).
- 1303 37. Huang, R.X. & Zhou, P.K. DNA damage response signaling pathways and targets for  
1304 radiotherapy sensitization in cancer. *Signal Transduct Target Ther* **5**, 60 (2020).
- 1305 38. Canman, C.E. *et al.* Activation of the ATM kinase by ionizing radiation and  
1306 phosphorylation of p53. *Science* **281**, 1677-1679 (1998).
- 1307 39. Tribius, S., Pidel, A. & Casper, D. ATM protein expression correlates with  
1308 radioresistance in primary glioblastoma cells in culture. *Int J Radiat Oncol Biol Phys*  
1309 **50**, 511-523 (2001).
- 1310 40. Ito, K. *et al.* Regulation of reactive oxygen species by Atm is essential for proper  
1311 response to DNA double-strand breaks in lymphocytes. *J Immunol* **178**, 103-110  
1312 (2007).
- 1313 41. Li, K. *et al.* ATM inhibition induces synthetic lethality and enhances sensitivity of  
1314 PTEN-deficient breast cancer cells to cisplatin. *Exp Cell Res* **366**, 24-33 (2018).
- 1315 42. Chen, J.H. *et al.* ATM-mediated PTEN phosphorylation promotes PTEN nuclear  
1316 translocation and autophagy in response to DNA-damaging agents in cancer cells.  
1317 *Autophagy* **11**, 239-252 (2015).
- 1318 43. Hartmann, O. *et al.* Implementation of CRISPR/Cas9 Genome Editing to Generate  
1319 Murine Lung Cancer Models That Depict the Mutational Landscape of Human  
1320 Disease. *Front Cell Dev Biol* **9**, 641618 (2021).
- 1321 44. Prieto-Garcia, C. *et al.* Maintaining protein stability of Np63 via USP28 is required by  
1322 squamous cancer cells. *EMBO Mol Med* **12**, e11101 (2020).
- 1323 45. Brunner, A. *et al.* PTEN and DNA-PK determine sensitivity and recovery in response  
1324 to WEE1 inhibition in human breast cancer. *Elife* **9** (2020).
- 1325 46. Szymonowicz, K., Oeck, S., Malewicz, N.M. & Jendrossek, V. New Insights into Protein  
1326 Kinase B/Akt Signaling: Role of Localized Akt Activation and Compartment-Specific  
1327 Target Proteins for the Cellular Radiation Response. *Cancers (Basel)* **10** (2018).
- 1328 47. Park, S. *et al.* PI-103, a dual inhibitor of Class IA phosphatidylinositide 3-kinase and  
1329 mTOR, has antileukemic activity in AML. *Leukemia* **22**, 1698-1706 (2008).
- 1330 48. Brinkmann, K., Schell, M., Hoppe, T. & Kashkar, H. Regulation of the DNA damage  
1331 response by ubiquitin conjugation. *Front Genet* **6**, 98 (2015).
- 1332 49. Marechal, A. & Zou, L. DNA damage sensing by the ATM and ATR kinases. *Cold Spring*  
1333 *Harb Perspect Biol* **5** (2013).
- 1334 50. Bhattacharya, S. & Asaithamby, A. Repurposing DNA repair factors to eradicate  
1335 tumor cells upon radiotherapy. *Transl Cancer Res* **6**, S822-S839 (2017).
- 1336 51. Medema, R.H. & Macurek, L. Checkpoint control and cancer. *Oncogene* **31**, 2601-  
1337 2613 (2012).
- 1338 52. Nikolaev, A. & Yang, E.S. The Impact of DNA Repair Pathways in Cancer Biology and  
1339 Therapy. *Cancers (Basel)* **9** (2017).
- 1340 53. Khanna, A. DNA damage in cancer therapeutics: a boon or a curse? *Cancer Res* **75**,  
1341 2133-2138 (2015).
- 1342 54. Wang, M. *et al.* Radiation Resistance in KRAS-Mutated Lung Cancer Is Enabled by  
1343 Stem-like Properties Mediated by an Osteopontin-EGFR Pathway. *Cancer Res* **77**,  
1344 2018-2028 (2017).
- 1345 55. Ruiz, E.J. *et al.* LUBAC determines chemotherapy resistance in squamous cell lung  
1346 cancer. *J Exp Med* **216**, 450-465 (2019).

- 1347 56. Sitthideatphaiboon, P. *et al.* LKB1 mutations in NSCLC are associated with  
1348 KEAP1/NRF2-dependent radiotherapy resistance targetable by glutaminase  
1349 inhibition. *Clin Cancer Res* (2020).
- 1350 57. McCabe, N. *et al.* Mechanistic Rationale to Target PTEN-Deficient Tumor Cells with  
1351 Inhibitors of the DNA Damage Response Kinase ATM. *Cancer Res* **75**, 2159-2165  
1352 (2015).
- 1353 58. Bazzichetto, C. *et al.* PTEN as a Prognostic/Predictive Biomarker in Cancer: An  
1354 Unfulfilled Promise? *Cancers (Basel)* **11** (2019).
- 1355 59. Hill, R. *et al.* PTEN loss accelerates KrasG12D-induced pancreatic cancer  
1356 development. *Cancer Res* **70**, 7114-7124 (2010).
- 1357 60. Rosenfeldt, M.T. *et al.* PTEN deficiency permits the formation of pancreatic cancer in  
1358 the absence of autophagy. *Cell Death Differ* **24**, 1303-1304 (2017).
- 1359 61. Ebbesen, S.H. *et al.* Pten loss promotes MAPK pathway dependency in HER2/neu  
1360 breast carcinomas. *Proc Natl Acad Sci U S A* **113**, 3030-3035 (2016).
- 1361 62. Cheng, H. *et al.* A genetic mouse model of invasive endometrial cancer driven by  
1362 concurrent loss of Pten and Lkb1 is highly responsive to mTOR inhibition. *Cancer Res*  
1363 **74**, 15-23 (2014).
- 1364 63. Iwanaga, K. *et al.* Pten inactivation accelerates oncogenic K-ras-initiated  
1365 tumorigenesis in a mouse model of lung cancer. *Cancer Res* **68**, 1119-1127 (2008).
- 1366 64. Kim, S.Y. *et al.* Doxorubicin-induced reactive oxygen species generation and  
1367 intracellular Ca<sup>2+</sup> increase are reciprocally modulated in rat cardiomyocytes. *Exp*  
1368 *Mol Med* **38**, 535-545 (2006).
- 1369 65. Perillo, B. *et al.* ROS in cancer therapy: the bright side of the moon. *Exp Mol Med* **52**,  
1370 192-203 (2020).
- 1371 66. Mohiuddin, I.S. & Kang, M.H. DNA-PK as an Emerging Therapeutic Target in Cancer.  
1372 *Front Oncol* **9**, 635 (2019).
- 1373 67. Kim, D., Liu, Y., Oberly, S., Freire, R. & Smolka, M.B. ATR-mediated proteome  
1374 remodeling is a major determinant of homologous recombination capacity in cancer  
1375 cells. *Nucleic Acids Res* **46**, 8311-8325 (2018).
- 1376 68. Lee, J.H. *et al.* ATM directs DNA damage responses and proteostasis via genetically  
1377 separable pathways. *Sci Signal* **11** (2018).
- 1378 69. McVey, M. & Lee, S.E. MMEJ repair of double-strand breaks (director's cut): deleted  
1379 sequences and alternative endings. *Trends Genet* **24**, 529-538 (2008).
- 1380 70. Milella, M. *et al.* PTEN: Multiple Functions in Human Malignant Tumors. *Front Oncol*  
1381 **5**, 24 (2015).
- 1382 71. Ma, J. *et al.* Inhibition of Nuclear PTEN Tyrosine Phosphorylation Enhances Glioma  
1383 Radiation Sensitivity through Attenuated DNA Repair. *Cancer Cell* **35**, 504-518 e507  
1384 (2019).
- 1385

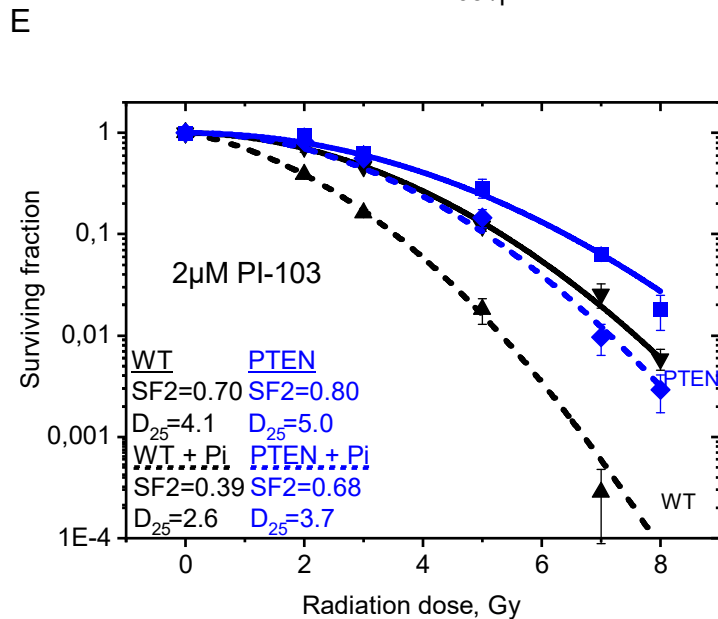
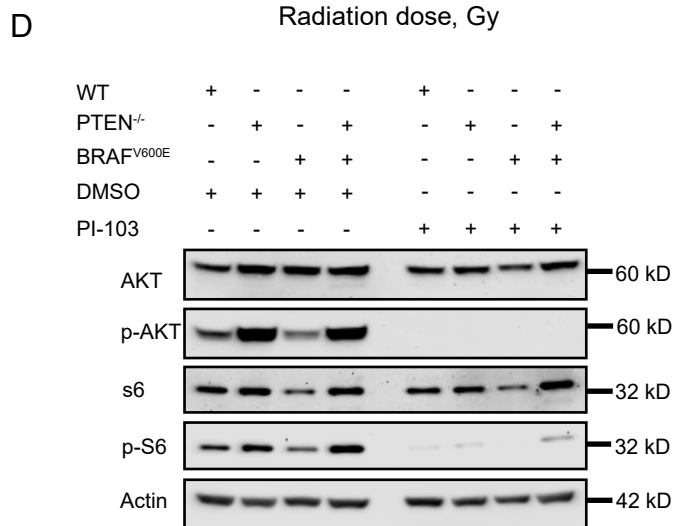
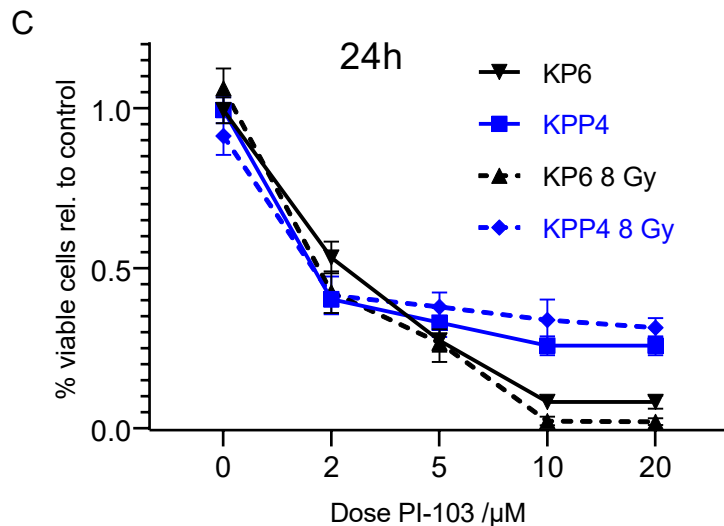
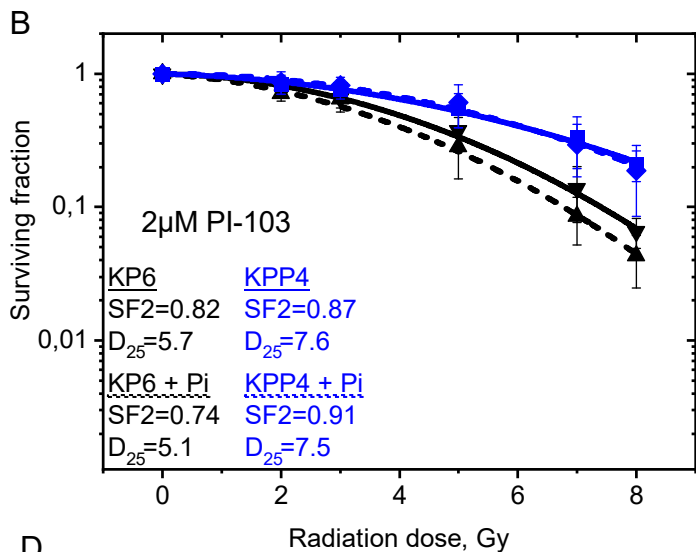
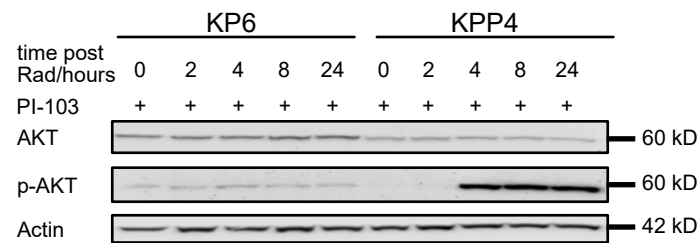
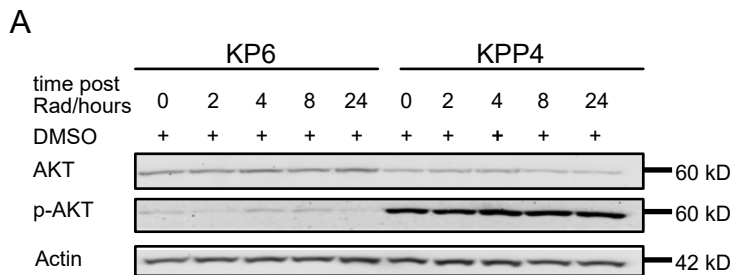






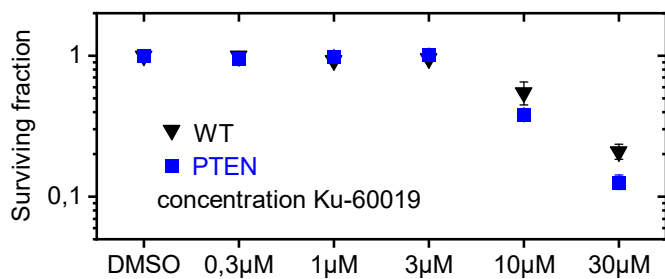


<i>Geneset</i>	<i>(N)ES</i>	<i>pValue</i>
GAMMA_Rad.	-1.67	<0.0005
DOXORUBICIN	-1.52	0.0158
KRAS_UP	2.15	<0.0005
AKT_MTOR_UP	-1.92	<0.0005
EMT	-2.20	<0.0005
METASTASIS_DN	-1,93	<0.0005



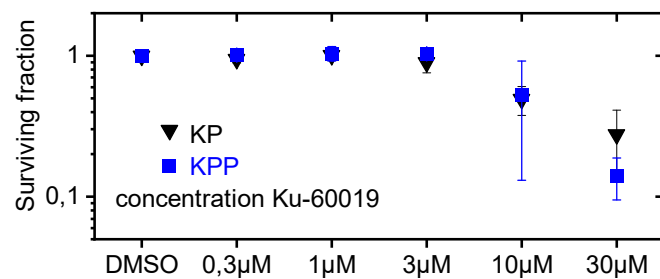
### BEAS-2B human tracheal cell line

A

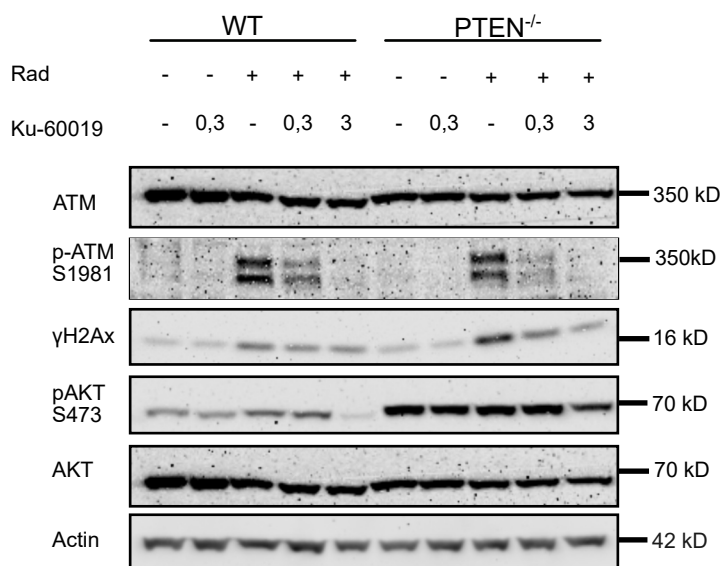


### primary mouse tumor cell line

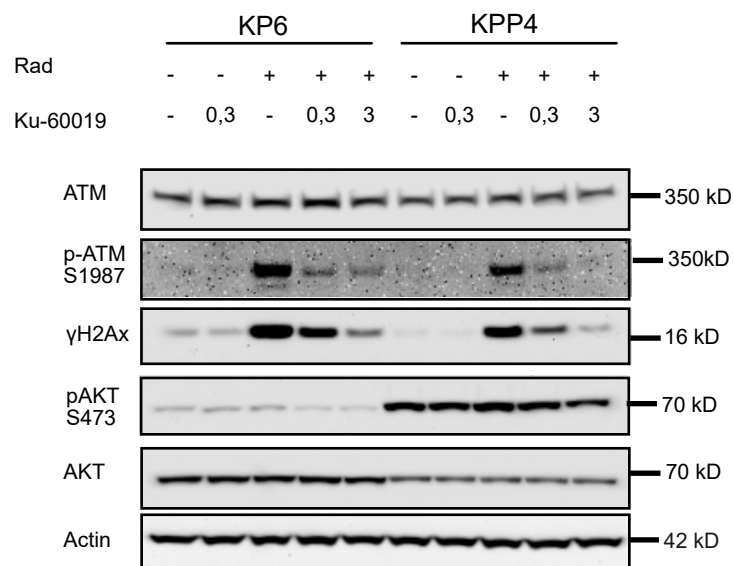
B



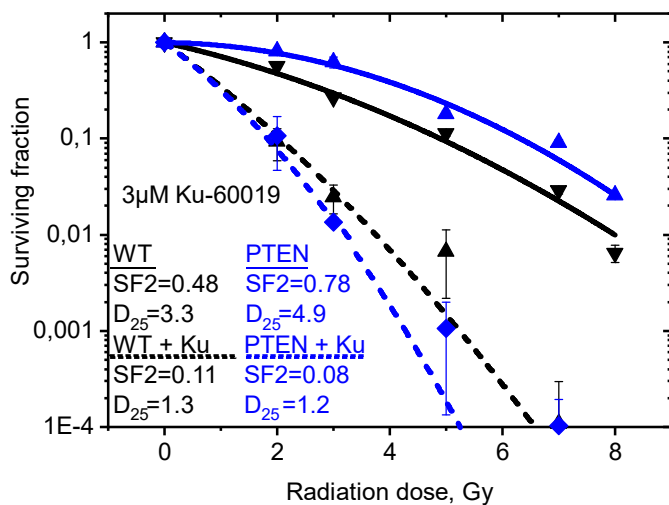
C



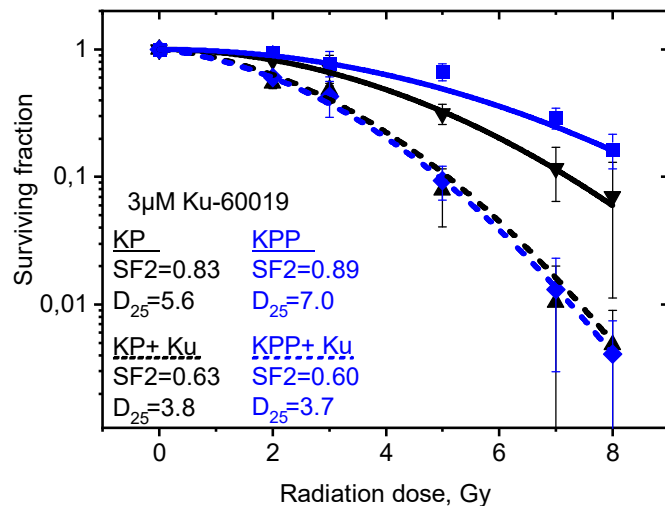
D

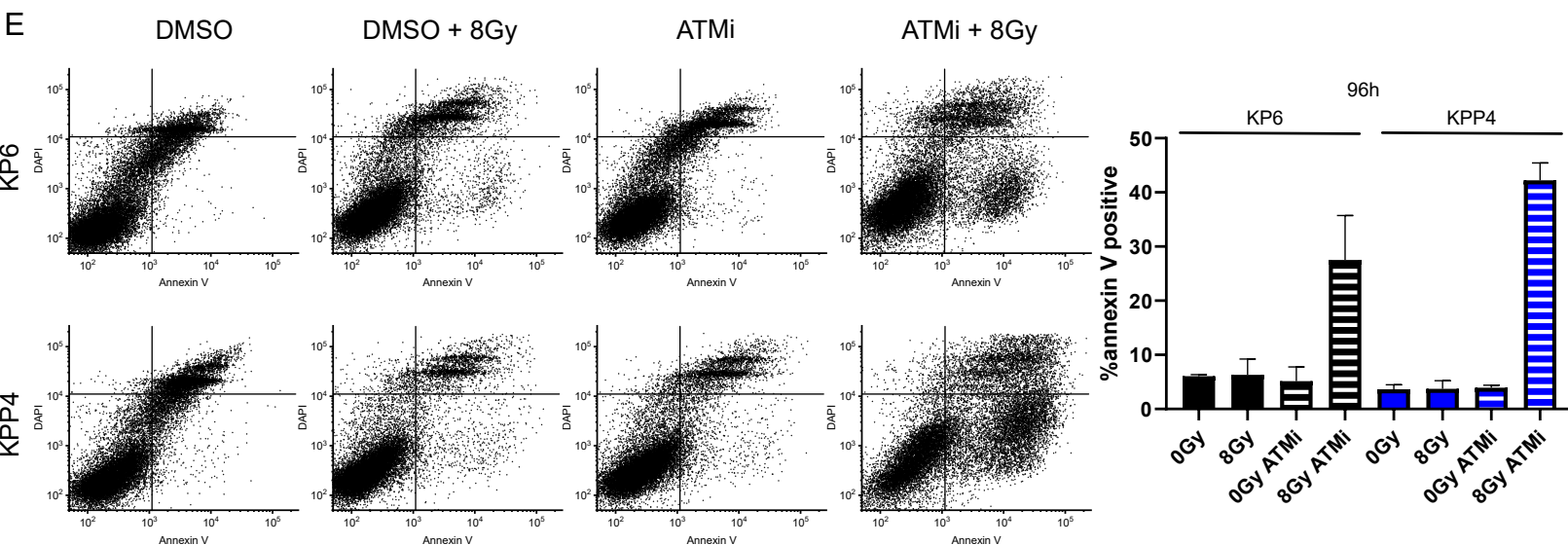
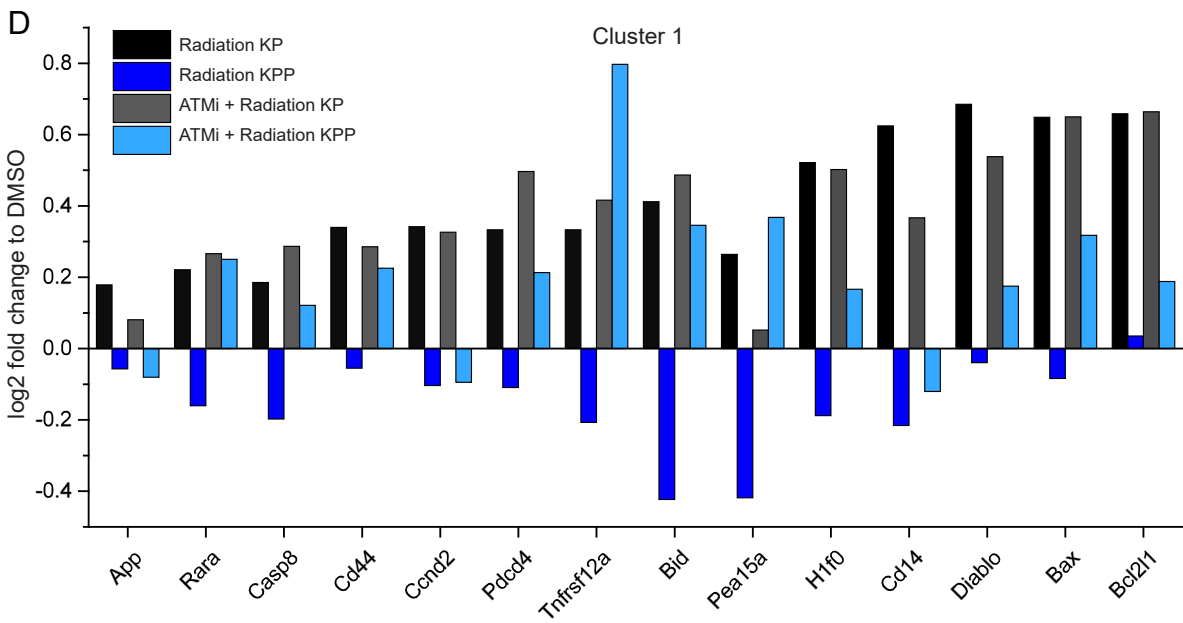
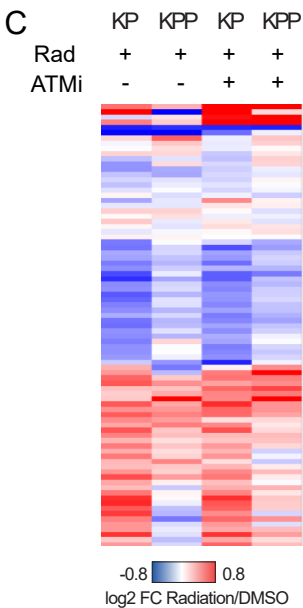
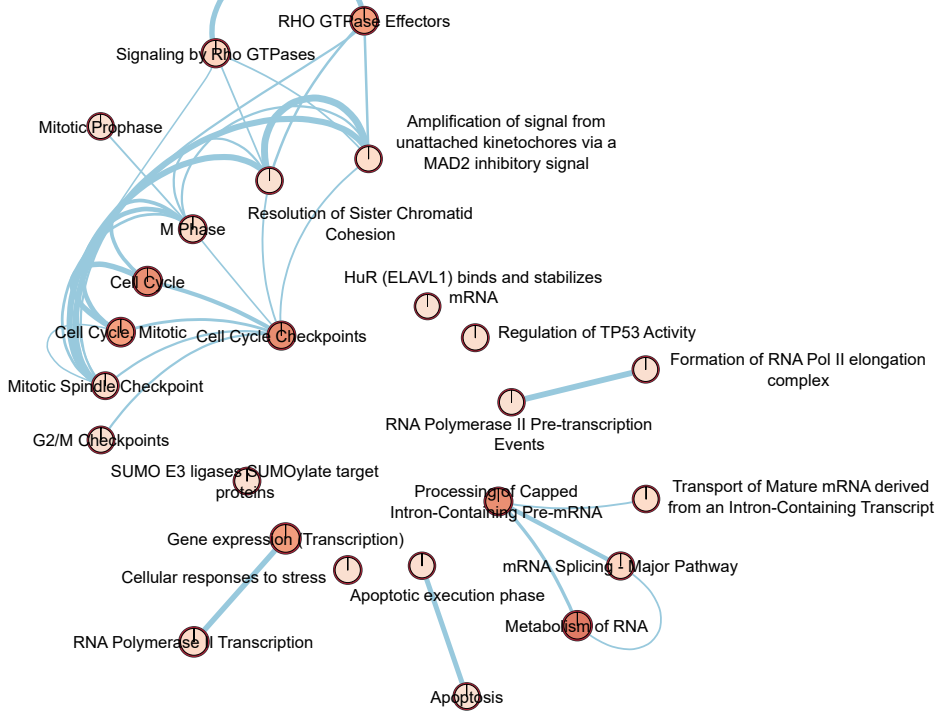
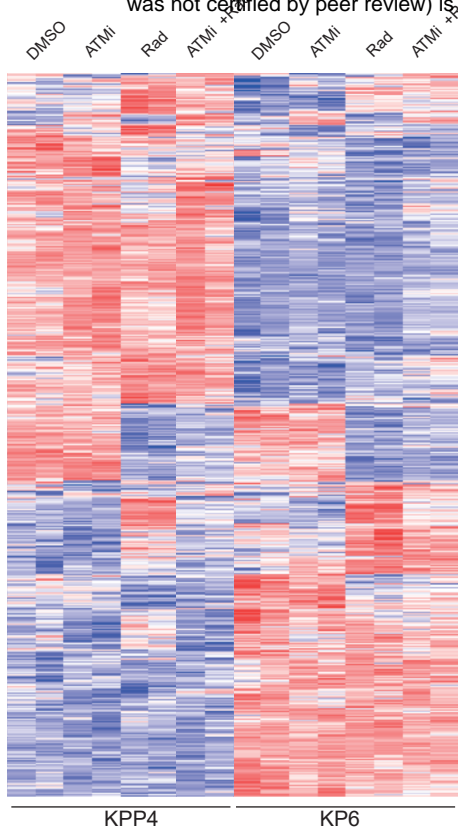


E



F





A

